Asociación Argentina
de Mecánica Computacional

Mecánica Computacional Vol XXXII, págs. 33-62 (artículo completo)
Carlos G. García Garino, Aníbal E. Mirasso, Mario A. Storti, Miguel E. Tornello (Eds.)
Mendoza, Argentina, 19-22 Noviembre 2013

ENERGY CONSERVING AND NUMERICAL STABILITY IN NON LINEAR DYNAMIC USING ISOGEOMETRIC ANALYSIS

Luis F. R. Espath, Alexandre L. Braun and Armando M. Awruch

Graduate Program in Civil Engineering (PPGEC), Federal University of Rio Grande do Sul (UFRGS), Av. Osvaldo Aranha, 99, 3o andar, 90035-190, Porto Alegre, RS, Brazil.
espath@gmail.com

Keywords: IsoGeometric Analysis; Generalized-α Method; Generalized Energy-Momentum Method + ξ; NURBS; Corotational Kinematics

Abstract. An investigation about energy conserving and numerical stability related to non linear dynamic problems involving large rotations and large displacements is carried out within the framework of IsoGeometric Analysis. A corotational kinematics derived from the exact polar decomposition is used in order to deal with geometrically non linear behavior. The Generalized α (Gα) and Generalized Energy-Momentum Method (GEMM+ξ) are employed with consistent and lumped mass, for a large range of continuity class of basis function. A set of examples are presented in order to show the accuracy and efficiency as well as the improvement of energy conserving and numerical stability.

1 INTRODUCTION

The manuscript presents an application of the so-called isogeometric analysis for the numerical solution of a non linear dynamic problems that involves large rotations and displacements. The use of standard techniques based on classical FE would incur large modelling errors associated with the high frequency range introduced by the spatial discretization, which are usually accounted for by introducing some sort of numerical dissipation.

The development of numerical algorithms to simulate the dynamic response of linear and nonlinear elastic bodies is a major topic in the field of elastodynamics. Traditional time-stepping schemes, which present excellent stability properties in the linear range, are frequently subject to numerical instabilities when they are applied to nonlinear problems using numerical models based on the finite element method (FEM). Therefore, investigations on elastodynamics using IsoGeometric analysis must be performed in order to study the influence of the IsoGeometric formulation over numerical issues such as stability and accuracy, where aspects related to the time integration process are also extremely important.

Isogeometric analysis is dedicated to unifying numerical techniques adopted in geometrical design and analysis, which is accomplished by using a single parameterization framework where the same basis functions are utilized in both procedures. Geometrical design and analysis have been performed independently with pre-processing programs based on computer aided design (CAD) technologies and numerical solvers based on the FEM. However, it is frequently observed that the finite element model obtained after mesh generation does not match the geometric shape of complex models reproduced with CAD tools, since insufficient approximations may be utilized depending on the basis functions adopted in the finite element formulation. Extending this remark to the field of dynamic analysis, one can also observe that the higher vibration modes of a dynamic response cannot be accurately represented due to modelling errors introduced when the spatial discretization procedure is applied to infinite-dimensional continuum systems, which may give rise to numerical instabilities if numerical dissipation is not adequately employed. In order to circumvent this drawback, IsoGeometric analysis may be utilized, where B-splines and NURBS are employed to build the geometric models and to approximate the solution field. The basic concepts on IsoGeometric analysis were introduced by Hughes et al. (2005) and many investigations have been performed in order to extend the applicability of the proposed formulation to different fields of computational applied mechanics (see, for instance, (Bazilevs et al., 2007; Benson et al., 2010; Kiendl et al., 2010)). A comprehensive work on IsoGeometric analysis may be found in Cottrell et al. (2009) and for additional information about B-spline and NURBS parameterizations, readers are addressed to Piegl and Tiller (1997).

The need for numerical dissipation was soon recognized when unconditional time stepping schemes were first applied to finite element models in order to solve dynamic problems with implicit algorithms. It was observed that large modeling errors associated with the high frequency range are introduced by the spatial discretization procedure owing to deficiencies found in the element formulation to reproduce the higher modes accurately. In this sense, although the standard Newmark's method presented no numerical dissipation, a formulation with controllable numerical damping was also proposed in Newmark (1959). Later, the Newmark's method and other early algorithms with numerical damping such as

the Wilson's method and the Houbolt's method were investigated in Goudreau and Taylor (1973), who recommended the introduction of a controlled degree of damping to reduce the spurious action of the higher modes. However, unconditionally stable algorithms lead to period elongation and the second-order accuracy is lost due to the introduction of numerical dissipation. This drawback was resolved with the method proposed by Hilber et al. (1977), which combines unconditional stability, second-order accuracy and numerical dissipation of higher modes. A similar improvement was obtained with the formulation introduced by Wood et al. (1980) and a generalization of the methods presented by Hilber et al. (1977) and Wood et al. (1980), the so-called generalized-α method, was provided by Chung and Hulbert (1993). The generalized-α method leads to second order accuracy and optimized behavior for the numerical dissipation is obtained when linear problems are analyzed, where minimal dissipation is observed for lower modes as well as maximal dissipation is verified for higher modes.

The development of energy-conserving algorithms were motivated by the work presented by Belytschko and Schoeberle (1975), who concluded that a numerical algorithm is stable in terms of energy if the sum of kinetic and internal energies within each time step is limited by the external work and the kinetic and internal energies evaluated in the previous time step. Moreover, it was verified that algorithms presenting unconditional stability for applications in linear dynamics are frequently subject to numerical instability when the nonlinear case is analyzed. Following the energy criterion introduced by Belytschko and Schoeberle (1975), Hughes et al. (1978) proposed an energy-conserving scheme for nonlinear dynamics where the trapezoidal rule is extended by using the Lagrange multiplier method to enforce energy conservation. Nevertheless, Ortiz (1986) demonstrated that energy conservation is not sufficient for maintaining numerical stability in the nonlinear range. Kuhl and Ramm (1996) also observed that the constraint energy method presented by Hughes et al. (1978) conserves the total energy perfectly, but leads to failure in the iteration procedure related to the Newton-Raphson linearization.

Indeed, Simo and Tarnow (1992) had already noticed the importance of momentum conservation by proposing the energy-momentum method, which conserves total energy as well as linear and angular momentum. Furthermore, second-order accuracy is also preserved. The energy-momentum method was developed considering the mid-point rule to evaluate the internal forces in every time step of the time integration process in order to reach energy conservation algorithmically, since it was concluded that the stress update procedure is crucial to obtain a numerical algorithm with energy-momentum conservation. The original formulation was introduced using a constitutive model for Saint Venant-Kirchoff materials, which was extended to arbitrary hyperelastic materials by Gonzalez (2000), who proposed a modified evaluation of the stress tensor employing discrete derivative to describe the required form for the algorithmic update of the second Piola-Kirchoff stress tensor. Later, Laursen and Meng (2001) reformulated the stress update scheme presented by Simo and Tarnow (1992) to account for general hyperelastic models properly, where some restrictions found in the original formulation were removed. An energy-momentum conserving algorithm for hypoelastic constitutive models was developed by Noels et al. (2004) by using a new expression for evaluating the internal forces at element level. Braun and Awruch (2008) also utilized a hypoelastic formulation for applications in nonlinear elastodynamics using the eight-node hexahedral element with one-point quadrature techniques. According to Romero (2012), there are infinite ways of obtaining second order accuracy as well as energy and momentum conservation algo-

rithms, whereas the characterization of the conserving stress as a minimization problem leads to that conclusion.

Although the conservation of energy and momentum is mandatory in order to obtain a stable numerical algorithm, it was also realized that some amount of numerical dissipation must be introduced in the model to damp out spurious contributions of the high-frequency range to the dynamic response, which are induced due to problems related to the finite element discretization of the spatial domain. On the other hand, it is well known that classical dissipative methods may fail when they are applied to nonlinear problems and loss of accuracy is generally observed in these cases. This situation motivated the development of energy dissipative momentum conserving algorithms, where momentum is conserved, energy dissipation is controlled and order of accuracy is maintained. Kuhl and Ramm (1996) proposed the constraint energy-momentum method, a time-stepping scheme combining conservation and dissipation properties, where energy and momentum are enforced considering the constraint energy methodology proposed by Hughes et al. (1978) and the generalized-α method (Chung and Hulbert, 1993) is utilized in order to obtain a dissipative time integration model. Optimized parameters for the α methods were determined leading to an integration process with less numerical dissipation for lower frequencies and more dissipation on higher frequencies of the energy spectrum. An algorithm based on controllable numerical dissipation and the energy-momentum method introduced by Simo and Tarnow (1992) was presented by Kuhl and Crisfield (1999) considering a nonlinear version of the generalized-α method. The numerical scheme was called generalized energy-momentum method and applications for shell dynamics were later investigated by Kuhl and Ramm (1999). Armero and Petocz (1998) and Crisfield et al. (1997) modified the energy-momentum method proposed by Simo and Tarnow (1992) to include numerical dissipation by using a damping parameter that only affects the second Piola-Kirchof stress tensor. Nevertheless, the so-called modified energy-momentum method is only first order accurate. In order to circumvent this drawback, Armero and Romero (2001b) developed a dissipative time-stepping algorithm with energy conservation properties that also preserves second order accuracy. Reviews on energy-momentum and dissipative methods may be found in Kuhl and Crisfield (1999); Armero and Romero (2001a); Erlicher et al. (2002).

In the present work, a numerical model based on IsoGeometric analysis is developed for applications in nonlinear elastodynamics for investigations on nonlinear elastostatics. The kinematic description of the continuum is performed using the corotational approach in the context of IsoGeometric analysis. A hypoelastic constitutive model is adopted utilizing corotational stress and strain tensors, where the small strain hypothesis and large displacements and rotations are considered. The numerical model is obtained by applying the Bubnov-Galerkin weighted residual method over the Cauchy's equation of motion and a Newton-Raphson scheme is adopted for linearization of the residual vector in the nonlinear range. Geometry and solution fields are approximated using NURBS basis functions according to the isoparametric concept. The Generalized-α Method and Generalized Energy-Momentum Method with an additional parameter (GEMM+ξ) are implemented into the IsoGeometric formulation in order to obtain stable and dissipative schemes for time integration. The influence of aspects related to the IsoGeometric discretization is investigated for numerical applications where numerical instabilities are expected when standard finite element models are utilized.

2 THEORETICAL ASPECTS

2.1 Governing equations for elastodynamics and corotational approach

Problems on elastodynamics may be formulated considering the Cauchy's equation of motion, where mass and energy conservation must be also enforced over the volume enclosing the body (see, for instance, Malvern (1969)). Considering a classical Lagrangian kinematical description in the Cartesian coordinate system and in the absence of temperature changes, the system of governing equations are reduced to the following expressions

$$\int_{\Omega_0} \rho\,(\underline{\mathbf{X}}, t_0)\ \mathrm{d}\Omega = \int_{\Omega} \rho\,(\underline{\mathbf{x}}, t)\ \mathrm{d}\Omega \quad \forall t \in [t_0, t] \tag{1a}$$

$$\rho\underline{\ddot{\mathbf{u}}} - \mathbf{div}\ \underline{\underline{\boldsymbol{\sigma}}} - \underline{\mathbf{b}} = \underline{\mathbf{0}} \quad \text{in} \quad \Omega \times [t_0, t] \tag{1b}$$

$$\underline{\mathbf{u}} = \overline{\underline{\mathbf{u}}} \quad \text{on} \quad \Gamma_D \times [t_0, t] \tag{1c}$$

$$\underline{\underline{\boldsymbol{\sigma}}} \cdot \underline{\mathbf{n}} = \overline{\underline{\mathbf{t}}} \quad \text{on} \quad \Gamma_N \times [t_0, t] \tag{1d}$$

$$\underline{\mathbf{u}}\,(\underline{\mathbf{x}}, t_0) = \overline{\underline{\mathbf{u}}}_0 \quad \text{in} \quad \Omega \tag{1e}$$

$$\underline{\dot{\mathbf{u}}}\,(\underline{\mathbf{x}}, t_0) = \overline{\underline{\dot{\mathbf{u}}}}_0 \quad \text{in} \quad \Omega \tag{1f}$$

where Equations (1a) and (1b) represent mass and momentum balances over the spatial domain $\Omega(t)$ corresponding to the body, respectively, with the first-order tensors $\underline{\mathbf{X}}$ and $\underline{\mathbf{x}}$ containing components of the material (X_i) and spatial (x_i) coordinates in the Cartesian coordinate system, t denotes time, ρ is the specific mass of the body, $\underline{\mathbf{b}}$ is the first-order tensor of body forces per unit mass, the second-order tensor $\underline{\underline{\boldsymbol{\sigma}}}$ contains components of the Cauchy stress tensor and the first-order tensors $\underline{\mathbf{u}}$ and $\underline{\ddot{\mathbf{u}}}$ are the displacement and the second time derivative of the displacement. The boundary conditions are given according to Equations (1c) and (1d), where the first-order tensors $\overline{\underline{\mathbf{u}}}$ and $\overline{\underline{\mathbf{t}}}$ are the prescribed Dirichlet and Neumann boundary conditions (Dirichlet: prescribed primitive variables - displacement prescribed) and (Neumann: prescribed derivatives of primitive variables - prescribed surface traction), over the boundaries Γ_D and Γ_N, respectively, taking into account that $\underline{\mathbf{n}}$ is the unit outward normal defined on boundary Γ_N. Equation (1e-1f) specifies the initial conditions ($t = t_0$; $\Omega = \Omega_0$) for the displacement and its first time derivative fields. In addition, $\Gamma_D \bigcup \Gamma_N = \Gamma$ and $\Gamma_D \bigcap \Gamma_N = \emptyset$. It is important to notice that the equilibrium equation, which is derived from the Cauchy's equation of motion, is defined taking into account the current deformed configuration of the body (Ω).

In the present model, geometrically nonlinear problems are analyzed taking into account the corotational approach (any tensor field in corotational frame are identified by $(\hat{\cdot})$), where stress and strain are described according to a coordinate system locally attached to every quadrature point. Consequently, a linear constitutive model restricted to small strains can be adopted in order to relate strain and stress measures, which may be written as

$$\underline{\underline{\hat{\boldsymbol{\sigma}}}} = \underline{\underline{\underline{\underline{\hat{\mathbf{C}}}}}}^{mat} : \underline{\underline{\hat{\boldsymbol{\epsilon}}}} = \lambda \mathrm{tr}(\underline{\underline{\hat{\boldsymbol{\epsilon}}}})\underline{\underline{\mathbf{1}}} + 2\mu\underline{\underline{\hat{\boldsymbol{\epsilon}}}} \tag{2}$$

where $\underline{\underline{\hat{\boldsymbol{\sigma}}}}$ and $\underline{\underline{\hat{\boldsymbol{\epsilon}}}}$ are the Cauchy stress tensor and the small strain tensor, both defined in the corotational system. $\underline{\underline{\underline{\underline{\hat{\mathbf{C}}}}}}^{mat}$ is the fourth-order elastic tensor, which may be described in terms of the Lamé constants, λ and μ. It is important to notice that when infinitesimal displacements and rotations are observed, the geometrical linear approach can be utilized and the undeformed configuration of the body (Ω_0) is taken as reference throughout the analysis.

Theoretically, the motion of a continuum can be decomposed into rigid body motion and pure deformation. This separation of rigid body and purely deformational motions is originated by assumption of large rotations. Once the spatial discretization of the problem is fine enough, this decomposition can be performed at the quadrature level, and consequently, in a corotational coordinate system, where the pure deformation part is always a small quantity with respect to the element dimensions. The corotational description maintains orthogonality of the reference frame, which leads to exact decomposition of the motion into rigid body and deformational parts. In this sense, an elastic constitutive formulation is very effective for corotational descriptions, since the nonlinear problem can be posed in rate form by considering the small strain hypothesis and an objective rate of the Cauchy stress tensor.

Assuming that all kinematical variables at the previous configuration t_n of the body are known, the displacement field at the end of the current load step can be obtained from integration of the strain rate tensor over the time interval defining the present load increment $[t_n, t_{n+1}]$. In addition, this integration to obtain the strain increment must be performed in the corotational coordinate system, where only the deformational part of the incremental displacement field is considered. The strain rate tensor in the corotational system is defined as:

$$\hat{\underline{\underline{\mathbf{d}}}} = \frac{1}{2}\left[\frac{\partial \hat{\underline{\mathbf{v}}}^{def}}{\partial \hat{\underline{\mathbf{x}}}} + \left(\frac{\partial \hat{\underline{\mathbf{v}}}^{def}}{\partial \hat{\underline{\mathbf{x}}}}\right)^{t}\right] \tag{3}$$

where $\hat{\underline{\mathbf{v}}}^{def}$ represents the velocity field associated with the deformation part of the motion in the corotational system. In order to obtain strain increments, some methodology must be adopted to integrate the strain tensor over the time interval $[t_n, t_{n+1}]$. In the present work, the mid-point integration proposed by Hughes and Winget (1980) is utilized, where the velocity is assumed to be constant within the time interval and the reference configuration is attached to the intermediate configuration $t_{n+\frac{1}{2}}$ in the corotational system. According to the mid-point integration, the strain increment may be obtained from:

$$\int_{t_n}^{t_{n+1}} \hat{\underline{\underline{\mathbf{d}}}}\, \mathrm{d}\tau = \frac{1}{2}\left[\frac{\partial \underline{\Delta\hat{\mathbf{u}}}^{def}}{\partial \hat{\underline{\mathbf{x}}}_{n+\frac{1}{2}}} + \left(\frac{\partial \underline{\Delta\hat{\mathbf{u}}}^{def}}{\partial \hat{\underline{\mathbf{x}}}_{n+\frac{1}{2}}}\right)^{t}\right] = \underline{\underline{\Delta\hat{\boldsymbol{\epsilon}}}} \tag{4}$$

where $\underline{\Delta\hat{\mathbf{u}}}^{def}$ is the deformation part of the displacement increment in the corotational system and $\hat{\underline{\mathbf{x}}}_{n+\frac{1}{2}}$ is the intermediate configuration of the body defined in the corotational system, which can be determined according to the following expression:

$$\hat{\underline{\mathbf{x}}}_{n+\frac{1}{2}} = \underline{\underline{\mathbf{R}}}_{n+\frac{1}{2}} \cdot \underline{\mathbf{x}}_{n+\frac{1}{2}} = \frac{1}{2}\underline{\underline{\mathbf{R}}}_{n+\frac{1}{2}} \cdot (\underline{\mathbf{x}}_n + \underline{\mathbf{x}}_{n+1}) \tag{5}$$

where $\underline{\underline{\mathbf{R}}}_{n+\frac{1}{2}}$ is the orthogonal transformation tensor performing rotation from the global system to the corotational system defined locally at the intermediate configuration $t_{n+\frac{1}{2}}$. The displacement increment referring to the present time interval $[t_n, t_{n+1}]$ can be decomposed as follows:

$$\underline{\Delta\mathbf{u}} = \underline{\Delta\mathbf{u}}^{def} + \underline{\Delta\mathbf{u}}^{rot} \tag{6}$$

where $\underline{\Delta\mathbf{u}}^{def}$ and $\underline{\Delta\mathbf{u}}^{rot}$ are, respectively, the deformation and rotation parts of the displacement increment defined in the global coordinate system. It is important to notice that the decomposition described in Equation (6) is locally performed at element level.

The deformation displacement increment in the corotational system can be obtained from the following expression:

$$\underline{\Delta\hat{\mathbf{u}}}^{def} = \underline{\underline{\mathbf{R}}}_{n+\frac{1}{2}} \cdot \underline{\Delta\mathbf{u}}^{def} = \underline{\hat{\mathbf{x}}}_{n+1} - \underline{\hat{\mathbf{x}}}_{n} \tag{7}$$

where the transformation tensor $\underline{\underline{\mathbf{R}}}$ is evaluated at the intermediate configuration $t_{n+\frac{1}{2}}$ of the current time interval $[t_n, t_{n+1}]$, since the strain rate tensor must be referred to the body configuration at $t_{n+\frac{1}{2}}$. Coordinates corresponding to the previous and current configurations of the body in the corotational system are obtained with following transformations:

$$\underline{\hat{\mathbf{x}}}_{n} = \underline{\underline{\mathbf{R}}}_{n} \cdot \underline{\mathbf{x}}_{n}; \qquad \underline{\hat{\mathbf{x}}}_{n+1} = \underline{\underline{\mathbf{R}}}_{n+1} \cdot \underline{\mathbf{x}}_{n+1} \tag{8}$$

where $\underline{\underline{\mathbf{R}}}_{n}$ and $\underline{\underline{\mathbf{R}}}_{n+1}$ are orthogonal transformation tensors performing rotations from the global system to the corotational system defined locally at t_n and t_{n+1}, respectively.

After determining the strain increment in the corotational system, strain and stress updates can be performed with the following equations:

$$\underline{\underline{\hat{\boldsymbol{\epsilon}}}}_{n+1} = \underline{\underline{\hat{\boldsymbol{\epsilon}}}}_{n} + \underline{\underline{\Delta\hat{\boldsymbol{\epsilon}}}} \tag{9a}$$

$$\underline{\underline{\hat{\boldsymbol{\sigma}}}}_{n+1} = \underline{\underline{\hat{\boldsymbol{\sigma}}}}_{n} + \underline{\underline{\Delta\hat{\boldsymbol{\sigma}}}} \tag{9b}$$

where n and $n+1$ denote the previous and current configurations in the corotational system, respectively. It is well known that the Cauchy stress tensor in the corotational system is frame-invariant, since stress measures are not affected by rigid body motions, but the rate of the Cauchy stress tensor is not. Therefore, in order to obtain an incrementally objective constitutive formulation, the Jaumann rate tensor is adopted in this work, which may be described as follows:

$$\overset{\circ}{\underline{\underline{\hat{\boldsymbol{\sigma}}}}}^{J} = \underline{\underline{\dot{\hat{\boldsymbol{\sigma}}}}} + \underline{\underline{\hat{\boldsymbol{\sigma}}}} \cdot \underline{\underline{\hat{\boldsymbol{\Omega}}}} - \underline{\underline{\hat{\boldsymbol{\Omega}}}} \cdot \underline{\underline{\hat{\boldsymbol{\sigma}}}} \tag{10}$$

where spin tensor $\underline{\underline{\hat{\boldsymbol{\Omega}}}}$ is the antisymmetric part of the spatial velocity gradient tensor $\underline{\underline{\hat{\mathbf{L}}}}$ defined in the corotational system. The corotational spin tensor must be also integrated over the time interval $[t_n, t_{n+1}]$ considering the same mid-point rule adopted in Equation (4).

The orthogonal transformation tensor $\underline{\underline{\mathbf{R}}}$ may be evaluated using several methods. In the present work, a classical polar decomposition theorem is utilized, where spectral decomposition or eigenprojection of the right Cauchy-Green deformation tensor $\underline{\underline{\mathbf{C}}}$ is adopted to obtain the right stretch tensor $\underline{\underline{\mathbf{U}}}$.

Being the deformation gradient tensor defined as

$$\underline{\underline{\mathbf{F}}} = \frac{\partial \underline{\mathbf{x}}}{\partial \underline{\mathbf{X}}} \tag{11}$$

it can be decomposed uniquely (while $\det(\underline{\underline{\mathbf{F}}}) > 0$) into a symmetric part and an orthogonal part

$$\underline{\underline{\mathbf{F}}} = \underline{\underline{\mathbf{Q}}} \cdot \underline{\underline{\mathbf{U}}} = \underline{\underline{\mathbf{V}}} \cdot \underline{\underline{\mathbf{Q}}} \tag{12}$$

where $\underline{\underline{\mathbf{Q}}}$ is an orthogonal tensor and $\underline{\underline{\mathbf{U}}}$ and $\underline{\underline{\mathbf{V}}}$ are the right and left stretch tensors. Recall that the right Cauchy-Green deformation tensor is defined as

$$\underline{\underline{\mathbf{C}}} = \underline{\underline{\mathbf{F}}}^{t} \cdot \underline{\underline{\mathbf{F}}} \tag{13}$$

Then, taking into account Equation (12)

$$\underline{\underline{\mathbf{C}}} = \underline{\underline{\mathbf{U}}}^t \cdot \underline{\underline{\mathbf{Q}}}^t \cdot \underline{\underline{\mathbf{Q}}} \cdot \underline{\underline{\mathbf{U}}} = \underline{\underline{\mathbf{U}}}^2 \tag{14}$$

and from spectral decomposition or eigenprojection of $\underline{\underline{\mathbf{C}}}$, the following expression may be written

$$\underline{\underline{\mathbf{C}}} = \lambda_i^2 \, \underline{\mathbf{N}}_i \otimes \underline{\mathbf{N}}_i = \underline{\underline{\mathbf{U}}}^2 \tag{15}$$

where λ_i^2 and $\underline{\mathbf{N}}_i$ are eigenvalues and eigenvectors of $\underline{\underline{\mathbf{C}}}$, respectively. Then, the orthogonal tensor is evaluated as

$$\underline{\underline{\mathbf{Q}}} = \underline{\underline{\mathbf{F}}} \cdot \underline{\underline{\mathbf{U}}}^{-1} = \underline{\underline{\mathbf{F}}} \cdot \left(\lambda_i^{-1} \, \underline{\mathbf{N}}_i \otimes \underline{\mathbf{N}}_i \right) \tag{16}$$

The transformation tensor utilized in the corotational formulation is obtained considering that $\underline{\underline{\mathbf{R}}} = \underline{\underline{\mathbf{Q}}}^t$.

2.2 Weak Formulation

A numerical model based on IsoGeometric analysis may be constructed using variational principles in the same form as that utilized by the FEM, which are equivalent to consider the corresponding weak forms obtained from the Galerkin method applied to the governing equations. In elastodynamics the Hamilton's principle can be adopted according to the following expression:

$$\int_{t_0}^{t} \delta \left(K - \pi \right) \, \mathrm{d}t + \int_{t_0}^{t} \delta W_d \, \mathrm{d}t \tag{17}$$

with

$$K = \frac{1}{2} \int_\Omega \rho \underline{\dot{\mathbf{u}}} \cdot \underline{\dot{\mathbf{u}}} \, \mathrm{d}\Omega \quad \delta K = \int_\Omega \rho \delta \underline{\dot{\mathbf{u}}} \cdot \underline{\dot{\mathbf{u}}} \, \mathrm{d}\Omega \tag{18a}$$

$$\pi = \int_\Omega U(\underline{\underline{\boldsymbol{\epsilon}}}) \, \mathrm{d}\Omega - \int_\Omega \underline{\mathbf{u}} \cdot \underline{\mathbf{b}} \, \mathrm{d}\Omega - \int_\Gamma \underline{\mathbf{u}} \cdot \underline{\mathbf{t}} \, \mathrm{d}\Gamma \quad \delta\pi = \int_\Omega \underline{\underline{\delta\boldsymbol{\epsilon}}} : \underline{\underline{\boldsymbol{\sigma}}} \, \mathrm{d}\Omega - \int_\Omega \underline{\delta\mathbf{u}} \cdot \underline{\mathbf{b}} \, \mathrm{d}\Omega - \int_\Gamma \underline{\delta\mathbf{u}} \cdot \underline{\mathbf{t}} \, \mathrm{d}\Gamma \tag{18b}$$

$$W_d = - \int_\Omega \underline{\mathbf{u}} \cdot \underline{\mathbf{f}}_d \, \mathrm{d}\Omega \quad \delta W_d = - \int_\Omega \underline{\delta\mathbf{u}} \cdot \underline{\mathbf{f}}_d \, \mathrm{d}\Omega \tag{18c}$$

where K and π are the kinetic energy and the total potential energy, respectively, with δK and $\delta\pi$ denoting its corresponding variations, W_d is the work done by any nonconserving force of the system and δW_d is the respective variation, $U(\underline{\underline{\boldsymbol{\epsilon}}}) = \int_\Omega \underline{\underline{\boldsymbol{\sigma}}} : \underline{\underline{\boldsymbol{\epsilon}}} \, \mathrm{d}\Omega$ is the strain energy density function and $\underline{\mathbf{f}}_d$ is the vector of nonconserving forces, including viscous damping $\underline{\mathbf{f}}_d = \chi \underline{\dot{\mathbf{u}}}$. The displacement variations $\underline{\delta\mathbf{u}}$ must vanish at the time limits t_0 and t_f and also on boundary Γ_D, where Dirichlet boundary conditions are imposed.

The semidiscrete system of momentum equations is obtained taking into account they are discrete in space but continuous in time. The space discretization is performed here considering the Bubnov-Galerkin method applied into the context of IsoGeometric analysis, where the displacement variations associated with the variational form (see Equation 17) assume the role of weight functions. By integrating by parts the kinetic energy variation presented in Equation 17 and considering the restrictions imposed on the displacement variations $\underline{\delta\mathbf{u}}$ at the time limits t_0 and t_f, the following expression is obtained:

$$\int_{t_0}^{t} \left(\int_{\Omega} \rho \underline{\delta \mathbf{u}} \cdot \underline{\ddot{\mathbf{u}}} \, \mathrm{d}\Omega + \int_{\Omega} \underline{\delta \mathbf{u}} \cdot \chi \underline{\dot{\mathbf{u}}} \, \mathrm{d}\Omega - \int_{\Omega} \underline{\underline{\delta \boldsymbol{\epsilon}}} : \underline{\underline{\boldsymbol{\sigma}}} \, \mathrm{d}\Omega + \int_{\Omega} \underline{\delta \mathbf{u}} \cdot \underline{\mathbf{b}} \, \mathrm{d}\Omega + \int_{\Gamma} \underline{\delta \mathbf{u}} \cdot \underline{\mathbf{t}} \, \mathrm{d}\Gamma \right) \mathrm{d}t = 0 \tag{19}$$

2.3 Spatial discretization – the IsoGeometric formulation using NURBS

In order to define the element concept in the context of IsoGeometric analysis, geometry, velocities, displacements and displacement variations must be discretized with the following expressions:

$$\begin{aligned} \underline{\mathbf{x}}(\underline{\boldsymbol{\xi}}, t) &= \sum_{a=1}^{n_{np}} R_a(\underline{\boldsymbol{\xi}}) \underline{\mathbf{x}}_a \qquad & \underline{\mathbf{u}}(\underline{\boldsymbol{\xi}}, t) &= \sum_{a=1}^{n_{np}} R_a(\underline{\boldsymbol{\xi}}) \underline{\mathbf{u}}_a \\ \underline{\ddot{\mathbf{u}}}(\underline{\boldsymbol{\xi}}, t) &= \sum_{a=1}^{n_{np}} R_a(\underline{\boldsymbol{\xi}}) \underline{\ddot{\mathbf{u}}}_a \qquad & \underline{\delta \mathbf{u}}(\underline{\boldsymbol{\xi}}, t) &= \sum_{a=1}^{n_{np}} R_a(\underline{\boldsymbol{\xi}}) \underline{\delta \mathbf{u}}_a \end{aligned} \tag{20}$$

where R_a is the NURBS basis function related to control point a, which is defined as function of the parametric coordinates (ξ, η, ζ), and n_{np} is the number of global control points (basis functions). Knot vectors corresponding to the different directions in the parametric space must be also specified defining the non-zero knot spans where elements are then identified. A three-dimensional knot vector $(\Xi, \mathcal{H}, \mathcal{Z})$ may be written as follows:

$$\begin{aligned} \Xi(\xi) &= \{\underbrace{0, \ldots, 0}_{p+1}, \xi_{p+1}, \ldots, \xi_{s_p - p - 1}, \underbrace{1, \ldots, 1}_{p+1}\}, \text{ with } s_p = n + p + 1 \\ \mathcal{H}(\eta) &= \{\underbrace{0, \ldots, 0}_{q+1}, \eta_{q+1}, \ldots, \eta_{s_q - q - 1}, \underbrace{1, \ldots, 1}_{q+1}\}, \text{ with } s_q = m + q + 1 \\ \mathcal{Z}(\zeta) &= \{\underbrace{0, \ldots, 0}_{r+1}, \zeta_{r+1}, \ldots, \zeta_{s_r - r - 1}, \underbrace{1, \ldots, 1}_{r+1}\}, \text{ with } s_r = l + r + 1 \end{aligned} \tag{21}$$

where p, q and r are the polynomial degrees of the basis functions over the parametric directions ξ, η and ζ respectively, and the corresponding numbers of basis functions are specified by $n + 1$, $m + 1$ and $l + 1$, respectively, which are also associated with the number of control points in the different directions of the physical space. Depending on the geometric topology of the problem, the knot vector may be reduced to two- or one-dimensional vectors, i.e., $(\Xi, \mathcal{H})$ or (Ξ).

The NURBS basis functions for three-dimensional applications are defined by:

$$R_{i,j,k}^{p,q,r}(\xi, \eta, \zeta) = \frac{N_{i,p}(\xi) \, N_{j,q}(\eta) \, N_{k,r}(\zeta) \, w_{i,j,k}}{\sum_{\hat{i},\hat{j},\hat{k}=0}^{n,m,l} N_{\hat{i},p}(\xi) \, N_{\hat{j},q}(\eta) \, N_{\hat{k},r}(\zeta) \, w_{\hat{i},\hat{j},\hat{k}}} \tag{22}$$

where the subscripts i, j and k indicate the position of the control point in the index space and the superscripts p, q and r define the polynomial degree of the basis functions. The weight term $w_{i,j,k}$ is related to the weight associated with the control point defined by the subindices i, j and k. Details on evaluation of functions may be found in Piegl and Tiller (1997) and Cottrell et al. (2009).

The Cox-de Boor recursive formulation (Cox (1972); deBoor (1972)) is usually adopted to evaluate B-spline basis functions, which are obtained considering a given one-dimensional

knot vector $\Xi(\xi)$ defined over the parametric space ξ, the number of control points defined along the corresponding direction in the physical space and the polynomial order of the corresponding basis functions. According to the Cox-de Boor formulation, the B-spline basis functions may be expressed as:

$$\begin{aligned} N_{i,0}\left(\xi\right) &= \begin{cases} 1 & \text{if } \xi_i \leqslant \xi < \xi_{i+1}, \\ 0 & \text{otherwise.} \end{cases} \\ N_{i,p}\left(\xi\right) &= \frac{\xi - \xi_i}{\xi_{i+p} - \xi_i} N_{i,p-1}\left(\xi\right) + \frac{\xi_{i+p+1} - \xi}{\xi_{i+p+1} - \xi_{i+1}} N_{i+1,p-1}\left(\xi\right) \end{aligned} \tag{23}$$

where p is the polynomial degree of the basis function $N(\xi)$ and i is the knot index. Equation (23) are straightforwardly extended to the basis functions associated with the parametric directions η and ζ.

The IsoGeometric model for the equation of motion given by Equation (19) can be written as:

$$\int_{t_0}^{t} \bigcup_{e=1}^{n_{el}} \left(\int_{\Omega} \rho \delta \underline{\mathbf{u}} \cdot \ddot{\underline{\mathbf{u}}} \, \mathrm{d}\Omega + \int_{\Omega} \underline{\delta \mathbf{u}} \cdot \chi \dot{\underline{\mathbf{u}}} \, \mathrm{d}\Omega - \int_{\Omega} \underline{\underline{\delta \boldsymbol{\epsilon}}} : \underline{\underline{\boldsymbol{\sigma}}} \, \mathrm{d}\Omega + \int_{\Omega} \underline{\delta \mathbf{u}} \cdot \underline{\mathbf{b}} \, \mathrm{d}\Omega + \int_{\Gamma} \underline{\delta \mathbf{u}} \cdot \underline{\mathbf{t}} \, \mathrm{d}\Gamma \right) \mathrm{d}t = 0 \tag{24}$$

where Ω_e and Γ_e are volume and boundary surface, respectively, corresponding to element e in the physical mesh. Considering $n+1$, $m+1$ and $l+1$ as the number of basis functions related to the parametric directions ξ, η and ζ, respectively, and their respective polynomial degrees denoted by p, q and r, element e is defined by determining the indices at which the corresponding non-zero knot span begins in the index space, that is:

$$e \in [\xi_i, \xi_{i+1}] \times [\eta_i, \eta_{i+1}] \times [\zeta_i, \zeta_{i+1}] \tag{25}$$

where $p+1 \leqslant i \leqslant n$, $q+1 \leqslant j \leqslant m$ and $r+1 \leqslant k \leqslant l$. The total number of elements, n_{el}, in which the spatial field is discretized in the parametric domain is defined as

$$n_{el} = (n-p+1) \cdot (m-q+1) \cdot (l-r+1) \tag{26}$$

By substituting the NURBS approximation related to the displacement field (see Equation (20)) into the constitutive equation (see Equation (20)), an element level approximation of the stress-strain relation, using Voigt notation, is obtained, where the strain components in the corotational system are given by:

$$\hat{\boldsymbol{\epsilon}} = \hat{\mathbf{B}} \cdot \hat{\mathbf{u}} \tag{27}$$

where $\hat{\mathbf{B}}$ and $\hat{\mathbf{u}}$ are the symmetric part of the gradient operator and the displacements field, respectively, which are evaluated referring to the current configuration of the body in the corotational coordinate system. When infinitesimal displacements and rotations are observed, Equation (27) is described in terms of the undeformed configuration of the body (Ω_0). Derivatives of the B-spline basis functions are represented in terms of B-spline lower order bases owing to the recursive definition of the basis functions. Algorithms for numerical evaluation of derivatives of B-spline basis functions may be found in Piegl and Tiller (1997).

Introducing the expansions shown in Equation (20) and the relationship given by Equation (27) into Equation (24), a matrix equation representing a system of algebraic equations is obtained for the equation of motion, which may be expressed as:

$$\bigcup_{e=1}^{n_{el}} \mathbf{M}^e \ddot{\mathbf{u}} + \bigcup_{e=1}^{n_{el}} \mathbf{C}^e \dot{\mathbf{u}} + \bigcup_{e=1}^{n_{el}} \mathbf{K}^e \mathbf{u} = \bigcup_{e=1}^{n_{el}} \mathbf{f}_{ext}^e \tag{28}$$

where $\mathbf{M}^e$ and $\mathbf{K}^e$ are the element mass and element stiffness matrices, respectively, and $\mathbf{f}_{ext}^e$ is the force vector at element level. The matrix and vector dimensions associated to $\mathbf{M}^e$ and $\mathbf{K}^e$, and $\mathbf{f}_{ext}^e$, are specified as $(n_{eq} \times n_{eq} \times n_{eq})$ and (n_{eq}), respectively, where $n_{eq} = n_{en} \times n_{dof}$, with n_{dof} denoting the number of degrees of freedom at the control point level. The union symbol indicates the assembling procedure to evaluate the global system of equations, considering the element contributions given according to connectivity relations established among the control points. The global stiffness matrix is always sparse because the support of each basis function is highly localized.

In the geometrically nonlinear regime, the system of equations represented by Equation (28) must be iteratively satisfied using the incremental approach (see Bathe (1996)), since internal forces are given now as functions of the current configuration of the body. The nonlinear equation of motion is obtained employing a linearization procedure given by the Newton-Raphson method, where the residual vector is submitted to a Taylor series expansion within the time interval $[t_n, t_{n+1}]$. Consequently, Equation (28) must be rewritten as follows:

$$\bigcup_{e=1}^{n_{el}} \mathbf{M}^e \ddot{\mathbf{u}} + \bigcup_{e=1}^{n_{el}} \mathbf{C}^e \dot{\mathbf{u}} + \bigcup_{e=1}^{n_{el}} \mathbf{K}_{tan}^e \left(\mathbf{u}^e\right) \Delta \mathbf{u} = \bigcup_{e=1}^{n_{el}} \mathbf{f}_{ext}^e - \bigcup_{e=1}^{n_{el}} \mathbf{f}_{int}^e \left(\mathbf{u}^e\right) \tag{29}$$

where $\mathbf{K}_{tan}^e$ is the tangent stiffness matrix. At each iterative step, the tangent stiffness matrix and the internal force vector are initially evaluated in the corotational coordinate system with the following expressions:

$$\hat{\mathbf{K}}_{tan}^e = \int_{\hat{\Omega}^e} \hat{\mathbf{B}}^t \left(\hat{\mathbf{C}}^{mat} + \hat{\mathbf{C}}^{geo}\right) \hat{\mathbf{B}} \, d\hat{\Omega}^e; \quad \hat{\mathbf{f}}_{int}^e = \int_{\hat{\Omega}^e} \hat{\mathbf{B}}^t \hat{\boldsymbol{\sigma}} \, d\hat{\Omega}^e \tag{30}$$

where $\hat{\Omega}^e$ is referenced to the current configuration of element e in the corotational coordinate system, $\hat{\mathbf{C}}$ and $\hat{\boldsymbol{\sigma}}$ are stress tensors related to the Jaumann rate tensor and the corotational Cauchy stress tensor, respectively, with both evaluated in the corotational coordinate system. In order to solve the system of nonlinear equilibrium equations, the tangent stiffness matrix and the internal force vector must be obtained in the global coordinate system through an objective transformation from the corotational system, that is:

$$\mathbf{K}_{tan}^e = \mathbf{R}^t \hat{\mathbf{K}}_{tan}^e \mathbf{R}; \quad \mathbf{f}_{int}^e = \mathbf{R}^t \hat{\mathbf{f}}_{int}^e \tag{31}$$

where $\mathbf{R}$ is the rotation matrix defined in the previous section.

2.4 Temporal integration – the Generalized-α method and Generalized Energy-Momentum Method + ξ

The time interval during which the dynamic analysis is carried out $[t_0, t_f]$ is subdivided into time steps $\Delta t = t_{n+1} - t_n$ in order to define the time step in the integration process for implicit algorithms, where the incremental approach is adopted. The kinematic variables

are assumed to be known at the beginning of every time step of the time integration and the same variables are obtained at the end of the respective time step considering the solution of the equation of motion, which is given in terms of displacement increments, and time approximations provided by a specific method, such as the Newmark's method. Although the Newmark's algorithm is unconditionally stable for linear problems, it may be unstable in the nonlinear range. In this sense, the generalized-α method may be utilized, where the equilibrium of the equation of motion is verified at an intermediate point of the time increment instead of the end point employed by the classical Newmark scheme.

It is assumed that $\mathbf{d}_{n+1} \approx \mathbf{u}(t_{n+1})$, $\mathbf{v}_{n+1} \approx \dot{\mathbf{u}}(t_{n+1})$ and $\mathbf{a}_{n+1} \approx \ddot{\mathbf{u}}(t_{n+1})$. At the beginning of each incremental step the predictor phase is defined according to the Newmark's Formulas

$$\begin{aligned} \mathbf{d}_{n+1}^{i} &= \tilde{\mathbf{d}}_{n+1} \\ \mathbf{v}_{n+1}^{i} &= \tilde{\mathbf{v}}_{n+1} \\ \mathbf{a}_{n+1}^{i} &= \tilde{\mathbf{a}}_{n+1} \end{aligned} \tag{32}$$

where

$$\tilde{\mathbf{d}}_{n+1} = \mathbf{d}_n + \Delta t \mathbf{v}_n + \frac{(\Delta t)^2}{2}\left((1-2\beta)\mathbf{a}_n + 2\beta\tilde{\mathbf{a}}_{n+1}\right) \tag{33a}$$

$$\tilde{\mathbf{v}}_{n+1} = \mathbf{v}_n + \Delta t\left((1-\gamma)\mathbf{a}_n + \gamma\tilde{\mathbf{a}}_{n+1}\right) \tag{33b}$$

The kinematic variables and residual of the governing equations are defined in the Gα and GEMM+ξ by using the following functions

$$\mathbf{R}\left(\mathbf{d}_{n+\alpha_f}, \mathbf{v}_{n+\alpha_f}, \mathbf{a}_{n+\alpha_m}\right) = \mathbf{0} \tag{34a}$$

$$\mathbf{d}_{n+\alpha_f} = \mathbf{d}_n + \alpha_f\left(\mathbf{d}_{n+1} - \mathbf{d}_n\right) \tag{34b}$$

$$\mathbf{v}_{n+\alpha_f} = \mathbf{v}_n + \alpha_f\left(\mathbf{v}_{n+1} - \mathbf{v}_n\right) \tag{34c}$$

$$\mathbf{a}_{n+\alpha_m} = \mathbf{a}_n + \alpha_m\left(\mathbf{a}_{n+1} - \mathbf{a}_n\right) \tag{34d}$$

with Newmark's Formulas (34e)

The equilibrium, Equation (34a), must be satisfied at the intermediate level. Once $(\mathbf{d}_n, \mathbf{v}_n, \mathbf{a}_n)$ is known, $\left(\mathbf{d}_{n+1}, \mathbf{v}_{n+1}, \mathbf{a}_{n+1}, \mathbf{d}_{n+\alpha_f}, \mathbf{v}_{n+\alpha_f}, \mathbf{a}_{n+\alpha_m}\right)$ can be obtained, where α_f, α_m, γ and β are parameters that define the method, which are selected in order to achieve second order accuracy and unconditional stability.

For second order linear differential equations with constant coefficients, Chung and Hulbert (1993) demonstrated that second order accuracy and unconditional stability are obtained with

$$\gamma = \frac{1}{2} - \alpha_f + \alpha_m \tag{35a}$$

$$\beta = \frac{1}{4}\left(1 - \alpha_f + \alpha_m\right)^2 \tag{35b}$$

In order to obtain a numerical damping control over the high frequencies, α_m and α_f must be defined as function of spectral radius ρ_∞. Chung and Hulbert (1993) established

that, for system with second order accuracy, one obtains

$$\alpha_m = \frac{2-\rho_\infty^c}{1+\rho_\infty^c} \tag{36a}$$

$$\alpha_f = \frac{1}{1+\rho_\infty^c} \tag{36b}$$

There is an additional dissipation parameter in the GEMM+ξ that displaces the internal force of the intermediate level defined by Gα, from $t_{n+\alpha_f} \rightarrow t_{n+\alpha+\xi}$. This parameter, Armero-Petocz parameter Armero and Petocz (1998) improves the stability.

$$\xi = \frac{1-\rho_\infty}{2+2\rho_\infty} \tag{37}$$

Assuming that the strain and stress tensors and all kinematical quantities are known at the end of the last time increment $t = t_n$, the solution at $t = t_{n+1}$ should be computed based on the converged solution at the previous time step. An algorithm describing all the calculation steps performed by the present numerical model is found below

1. ***Predictor Phase***:

   select a predictor according to the Newmark's formulas estimating $\left(\mathbf{d}^0_{n+1},\, \mathbf{v}^0_{n+1},\, \mathbf{a}^0_{n+1}\right)$ (38)

2. ***Corrector Phase***: loop over $i = 0, \ldots, i_{max}$

   (a) evaluate $\left(\mathbf{d}^i_{n+\alpha_f},\, \mathbf{v}^i_{n+\alpha_f},\, \mathbf{a}^i_{n+\alpha_m}\right)$

$$\mathbf{d}^i_{n+\alpha_f} = (1-\alpha_f)\,\mathbf{d}_n + \alpha_f \mathbf{d}^i_{n+1} \tag{39a}$$

$$\mathbf{v}^i_{n+\alpha_f} = (1-\alpha_f)\,\mathbf{v}_n + \alpha_f \mathbf{v}^i_{n+1} \tag{39b}$$

$$\mathbf{a}^i_{n+\alpha_m} = (1-\alpha_m)\,\mathbf{a}_n + \alpha_m \mathbf{a}^i_{n+1} \tag{39c}$$

   (b) Assembly the residual vector with variables at the intermediate level

$$\frac{\mathrm{d}\mathbf{R}^i}{\mathrm{d}\mathbf{d}_{n+1}}\Delta\mathbf{d} = -\mathbf{R}^i_{n+1} \tag{40}$$

   where

$$\begin{aligned} \mathbf{R}^i_{n+1} &= \mathbf{R}(\mathbf{d}^i_{n+\alpha_f},\, \mathbf{v}^i_{n+\alpha_f},\, \mathbf{a}^i_{n+\alpha_m}) \\ {}^{\mathrm{G}\alpha}\mathbf{R}^i_{n+1} &= \mathbf{M}\mathbf{a}^i_{n+\alpha_m} + \mathbf{C}\mathbf{v}^i_{n+\alpha_f} + {}^{\mathrm{G}\alpha}\mathbf{N}^i_{n+\alpha_f} - \mathbf{f}^{ext}_{n+\alpha_f} \\ {}^{\mathrm{GEMM}+\xi}\mathbf{R}^i_{n+1} &= \mathbf{M}\mathbf{a}^i_{n+\alpha_m} + \mathbf{C}\mathbf{v}^i_{n+\alpha_f} + {}^{\mathrm{GEMM}+\xi}\mathbf{N}^i_{n+\alpha_f+\xi} - \mathbf{f}^{ext}_{n+\alpha_f} \end{aligned} \tag{41}$$

   $\mathbf{N}$ is the internal force vector and $\mathbf{f}^{ext}_{n+\alpha_f} = (1-\alpha_f)\,\mathbf{f}^{ext}_n + \alpha_f \mathbf{f}^{ext}_{n+1}$ is the external load vector evaluated at generalized intermediate point. The following expression

$$\frac{\mathrm{d}\mathbf{R}^i}{\mathrm{d}\mathbf{d}_{n+1}} = \frac{\mathrm{d}\mathbf{R}}{\mathrm{d}\mathbf{d}_{n+1}}(\mathbf{d}^i_{n+\alpha_f},\, \mathbf{v}^i_{n+\alpha_f},\, \mathbf{a}^i_{n+\alpha_m}) \tag{42}$$

   is the total derivative ($\frac{\mathrm{d}\mathbf{R}}{\mathrm{d}\mathbf{d}_{n+1}}$), which is presented in Equations (44) and (45).

(c) with the solution of Equation (40), kinematic variables are updated

$$\begin{aligned}\mathbf{d}_{n+1}^{i+1} &= \mathbf{d}_{n+1}^{i} + \Delta\mathbf{d} \\ \mathbf{v}_{n+1}^{i+1} &= \mathbf{v}_{n+1}^{i} + \frac{\gamma}{\beta\Delta t}\Delta\mathbf{d} \\ \mathbf{a}_{n+1}^{i+1} &= \mathbf{a}_{n+1}^{i} + \frac{1}{\beta(\Delta t)^2}\Delta\mathbf{d}\end{aligned} \tag{43}$$

3. ***Check convergence***: If the criterion is not satisfied, return to step 1, with $i = i+1$. Otherwise, go forward to the next time step.

The total derivative of Equation (42) is obtained as follow

$$\begin{aligned}\frac{\mathrm{d}\mathbf{R}}{\mathrm{d}\mathbf{d}_{n+1}} =& \frac{\mathrm{d}\mathbf{R}}{\mathrm{d}\mathbf{d}_{n+\alpha_f}}\frac{\mathrm{d}\mathbf{d}_{n+\alpha_f}}{\mathrm{d}\mathbf{d}_{n+1}} \\ &+ \frac{\mathrm{d}\mathbf{R}}{\mathrm{d}\mathbf{v}_{n+\alpha_f}}\frac{\mathrm{d}\mathbf{v}_{n+\alpha_f}}{\mathrm{d}\mathbf{v}_{n+1}}\frac{\mathrm{d}\mathbf{v}_{n+1}}{\mathrm{d}\mathbf{d}_{n+1}} \\ &+ \frac{\mathrm{d}\mathbf{R}}{\mathrm{d}\mathbf{a}_{n+\alpha_m}}\frac{\mathrm{d}\mathbf{a}_{n+\alpha_m}}{\mathrm{d}\mathbf{a}_{n+1}}\frac{\mathrm{d}\mathbf{a}_{n+1}}{\mathrm{d}\mathbf{d}_{n+1}}\end{aligned} \tag{44}$$

and from Equations (33) and (38), one obtain

$$\frac{\mathrm{d}\mathbf{R}}{\mathrm{d}\mathbf{d}_{n+1}} = \frac{\alpha_m}{\beta(\Delta t)^2}\mathbf{M} + \frac{\gamma\alpha_f}{\beta\Delta t}\mathbf{C} + \mathbf{K}_{tan} \tag{45}$$

In Gα method the internal force and tangent stiffness matrix at generalized intermediate point are evaluated accordingly with the following expression:

$${}^{\mathrm{G}\alpha}\mathbf{N}_{n+\alpha_f}^{i} = (1-\alpha_f)\int_{\hat{\Omega}} \hat{\mathbf{B}}^t(\hat{\mathbf{u}}_n)\,\hat{\boldsymbol{\sigma}}(\hat{\mathbf{u}}_n)\,\mathrm{d}\hat{\Omega} + \alpha_f\int_{\hat{\Omega}} \hat{\mathbf{B}}^t(\hat{\mathbf{u}}_{n+1})\,\hat{\boldsymbol{\sigma}}(\hat{\mathbf{u}}_{n+1})\,\mathrm{d}\hat{\Omega} \tag{46}$$

$$\begin{aligned}{}^{\mathrm{G}\alpha}\mathbf{K}_{n+\alpha_f}^{tan} =& \alpha_f\,(K_m + K_g) \\ =& \alpha_f\int_{\hat{\Omega}} \hat{\mathbf{B}}^t(\hat{\mathbf{u}}_{n+1})\left(\hat{\mathbf{C}}^{mat} + \hat{\mathbf{C}}^{geo}(\hat{\mathbf{u}}_{n+1})\right)\hat{\mathbf{B}}(\hat{\mathbf{u}}_{n+1})\,\mathrm{d}\hat{\Omega}\end{aligned} \tag{47}$$

while in GEMM+ξ method the internal force and tangent stiffness matrix at generalized intermediate point are evaluated accordingly with the following expression:

$${}^{\mathrm{GEMM}+\xi}\mathbf{N}_{n+\alpha_f+\xi}^{i} = \int_{\hat{\Omega}} \hat{\mathbf{B}}^t(\hat{\mathbf{u}}_{n+\alpha_f})\left[(\alpha_f-\xi)\,\hat{\boldsymbol{\sigma}}(\hat{\mathbf{u}}_n) + (\alpha_f+\xi)\,\hat{\boldsymbol{\sigma}}(\hat{\mathbf{u}}_{n+1})\right]\mathrm{d}\hat{\Omega} \tag{48}$$

$$\begin{aligned}{}^{\mathrm{GEMM}+\xi}\mathbf{K}_{n+\alpha_f+\xi}^{tan} &= (\alpha_f+\xi)\,K_m + \alpha_f K_g \\ &= (\alpha_f+\xi)\int_{\hat{\Omega}} \hat{\mathbf{B}}^t(\hat{\mathbf{u}}_{n+\alpha_f})\hat{\mathbf{C}}^{mat}\hat{\mathbf{B}}(\hat{\mathbf{u}}_{n+1})\,\mathrm{d}\hat{\Omega} \\ &\quad + \alpha_f\int_{\hat{\Omega}} \hat{\mathbf{B}}^t(\hat{\mathbf{u}}_{n+\alpha_f})\hat{\mathbf{C}}^{geo}(\hat{\mathbf{u}}_{n+\alpha_f})\hat{\mathbf{B}}(\hat{\mathbf{u}}_{n+\alpha_f})\,\mathrm{d}\hat{\Omega} \\ &\approx (\alpha_f+\xi)\int_{\hat{\Omega}} \hat{\mathbf{B}}^t(\hat{\mathbf{u}}_{n+\alpha_f})\hat{\mathbf{C}}^{mat}\hat{\mathbf{B}}(\hat{\mathbf{u}}_{n+\alpha_f})\,\mathrm{d}\hat{\Omega} \\ &\quad + \alpha_f\int_{\hat{\Omega}} \hat{\mathbf{B}}^t(\hat{\mathbf{u}}_{n+\alpha_f})\hat{\mathbf{C}}^{geo}(\hat{\mathbf{u}}_{n+\alpha_f})\hat{\mathbf{B}}(\hat{\mathbf{u}}_{n+\alpha_f})\,\mathrm{d}\hat{\Omega}\end{aligned} \tag{49}$$

It is important to notice that material contribution into tangent stiffness matrix is modified in order to get a symmetry matrix.

2.5 Total energy, linear and angular momentum

There are some quantities that have a great importance in structural dynamics, such as: total energy, linear and angular momentum, in order to judge the stability and conservative properties. The total energy E is composed as kinetic energy K and internal strain energy U

$$E = K + U \tag{50a}$$

$$K = \int_{\Omega} \rho \underline{\dot{\mathbf{u}}} \cdot \underline{\dot{\mathbf{u}}} \, \mathrm{d}\Omega \tag{50b}$$

$$E = \int_{\Omega} \underline{\underline{\boldsymbol{\sigma}}} : \underline{\underline{\boldsymbol{\epsilon}}} \, \mathrm{d}\Omega \tag{50c}$$

The linear and angular momentum can be evaluated as

$$L = \int_{\Omega} \rho \underline{\dot{\mathbf{u}}} \, \mathrm{d}\Omega \tag{51a}$$

$$J = \int_{\Omega} \rho \underline{\mathbf{u}} \times \underline{\dot{\mathbf{u}}} \, \mathrm{d}\Omega \tag{51b}$$

3 NUMERICAL APPLICATION

3.1 Flying toss rule

This problem was study by Kuhl and Ramm (1996), where different time-integration schemes are employed to understand the numerical dissipation and its stability. A numerical investigation of the plane movement of a toss rule is performed in this example, where a geometrically nonlinear dynamic analysis is carried out. Geometry and boundary conditions are shown in Figure 1a, load description for the present simulation is shown in Figure 1b and material properties of the structure as well as the time step adopted in the time integration procedure are found in Table 1. It is important to notice that distributed loads are applied to the structure to produce the plane motion of the rule, which is free to fly in the absence of displacement restrictions and gravity action. Computational parameters regarding the numerical analyses performed here are presented in Table 2. Number and distribution (L, h, z) of elements over the physical space referring to the rule are again given according to the continuity class, where the element configurations $(16 \times 1 \times 1)$, $(21 \times 1 \times 1)$, $(31 \times 1 \times 1)$ and $(61 \times 1 \times 1)$ correspond to the continuity classes C^1, C^2, C^3 and C^4, respectively. The adopted convergence criteria is $2 \cdot 10^{-8}$.

The dynamic responses obtained from the numerical analyses performed here are shown in Figures 3, 4 and 5 for Gα with consistent mass, in Figures 6, 7 and 8 for Gα with lumped mass, in Figures 9, 10 and 11 for GEMM+ξ with consistent mass, in Figures 12, 13 and 14 for GEMM+ξ with lumped mass, which correspond to time histories referring to the respective energy budget, linear and angular momentum.

The results shown here demonstrate again a sudden interruption of the time integration process when a spectral radius equal to $\rho_\infty = 1.00$ is considered (no numerical dissipation), independently of the continuity class utilized, for Gα method with consistent mass, whereas for lumped mass the convergence is reached only for C^1 and C^2, and with the increase of continuity the numerical instability is anticipated. In this sense, the influence of the continuity class on the energy response was not identified for consistent mass. On the other hand, stable solutions can be obtained even with small amounts of numerical dissipation, i.e. $\rho_\infty = 0.99$, where the total energy is perfectly maintained during the

Table 1: Geometrical and load characteristics for the toss rule analysis

Young modulus - $E\left[N/m^2\right]$	$2.06 \cdot 10^{11}$
Poisson coefficient - ν	0.3
Specific mass - $\rho\left[kg/m^3\right]$	$7.8 \cdot 10^3$
Damping coefficient - ϕ	0.0
Time step - $\Delta t\,[s]$	$1.0 \cdot 10^{-4}$

time interval of the numerical analysis. The same behavior was observed for the components of the angular and linear momentum. For analyses carried out with GEMM+ξ with consistent and lumped mass is achieved a stable analysis and with conserving energy and momentum. The range of stable spectral radius obtained with the IsoGeometric model is slightly wider that that presented by the finite element model proposed by Braun and Awruch (2008). The energy responses obtained here are in agreement with the numerical predictions presented by Kuhl and Ramm (1999). In Kuhl and Ramm (1999) is evidenced that Gα is not stable and cannot conserve the energy-momentum.

The motion referring to the toss rule can be visualized in Figure 2, where a sequence of deformed configurations obtained with the algorithm proposed is shown for Gα method. One can observe that the inertial motion is developed after the initial load is removed. Structural displacements take place on a plane in accordance with the load configuration prescribed initially. In Figure 2a is presented successive configurations from $t = 0.0$ to $t = 0.1$ with $\Delta t = 0.001$, while in Figure 2b is presented successive configurations from $t = 0.0$ to $t = 0.03$ with $\Delta t = 0.0001$ for Gα method, for continuity class C^4 and C^1, respectively.

It is presented in Table 4 the numerical dissipation at the end of each analysis over each spectral radius and continuity class. It is observed that there is not a dependency between the conservation of the total energy, linear, angular momentum and the continuity class. On other hand, the stability shows a different behavior with respect to the first example. For Gα with consistent mass, there is not a dependency between the stability and the continuity class. While for Gα with lumped mass seems that the instability is postponed when the continuity class is reduced.

In Kuhl and Ramm (1996); Kuhl and Crisfield (1999); Kuhl and Ramm (1999) a parametric study is carried out in function of spectral radius for several time integration methods, such as, Constrained Energy-Momentum Method Kuhl and Ramm (1996), Energy-Momentum Method, Generalized Energy-Momentum Method Kuhl and Ramm (1999), Modified Energy-Momentum Method and Generalized-α Method. For any time integrator scheme is possible to see a deterioration of the solution in terms of energy budget and momentum conservation with the increase of the spectral radius.

It was observed that the convergence rate of this analysis is about 1.9 and 2.1 for force and displacement convergence, respectively, in Gα method, while in GEMM+ξ method is observed a convergence rate about 1.7 and 1.9 for force and displacement convergence, respectively. The convergence itself present indifferent in front of consistent and lumped mass.

Table 2: Computational parameters employed in the toss rule analysis

Control mesh (L, h, z)	Continuity class	Spectral radius - ρ_∞	Degrees (p, q, r)
	Gα consistent mass		
$66 \times 3 \times 2$	C^1	$0.50; 0.95; 0.99; 1.00$	$5, 2, 1$
$66 \times 3 \times 2$	C^2	$0.50; 0.95; 0.99; 1.00$	$5, 2, 1$
$66 \times 3 \times 2$	C^3	$0.50; 0.95; 0.99; 1.00$	$5, 2, 1$
$66 \times 3 \times 2$	C^4	$0.50; 0.95; 0.99; 1.00$	$5, 2, 1$
	Gα lumped mass		
$66 \times 3 \times 2$	C^1	1.00	$5, 2, 1$
$66 \times 3 \times 2$	C^2	1.00	$5, 2, 1$
$66 \times 3 \times 2$	C^3	1.00	$5, 2, 1$
$66 \times 3 \times 2$	C^4	1.00	$5, 2, 1$
	GEMM+ξ consistent mass		
$66 \times 3 \times 2$	C^1	1.00	$5, 2, 1$
$66 \times 3 \times 2$	C^2	1.00	$5, 2, 1$
$66 \times 3 \times 2$	C^3	1.00	$5, 2, 1$
$66 \times 3 \times 2$	C^4	1.00	$5, 2, 1$
	GEMM+ξ lumped mass		
$66 \times 3 \times 2$	C^1	1.00	$5, 2, 1$
$66 \times 3 \times 2$	C^2	1.00	$5, 2, 1$
$66 \times 3 \times 2$	C^3	1.00	$5, 2, 1$
$66 \times 3 \times 2$	C^4	1.00	$5, 2, 1$

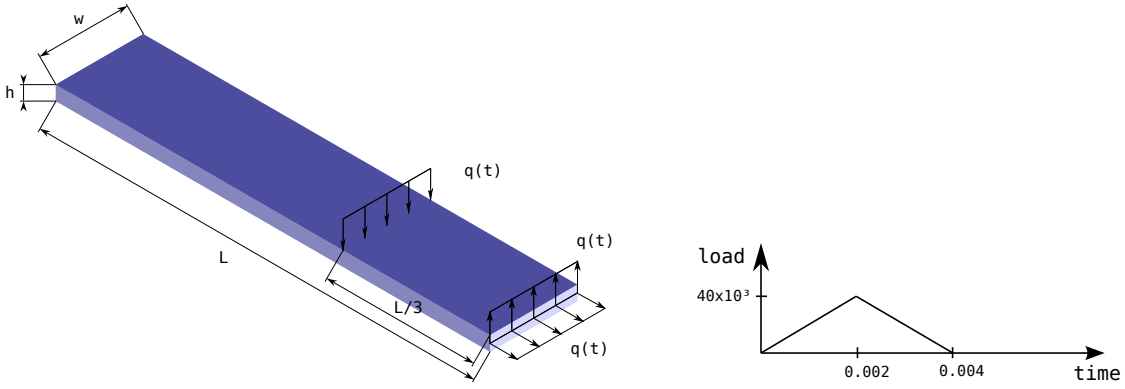

(a) Geometry and boundary conditions (b) Load $q(t)$

Figure 1: Geometry and boundary conditions of the toss rule.

Table 3: Convergence and failure time.

ρ_∞	C^1	C^2	C^3	C^4
		Gα consistent mass		
0.50	conv.	conv.	conv.	conv.
0.95	conv.	conv.	conv.	conv.
0.99	conv.	conv.	conv.	fail at $t_f = 0.9040s$
1.00	fail at $t_f = 0.5340s$	fail at $t_f = 0.7260s$	fail at $t_f = 0.4935s$	fail at $t_f = 0.5375s$
		Gα lumped mass		
1.00	conv.	conv.	fail at $t_f = 0.7775s$	fail at $t_f = 0.6115s$
		GEMM+ξ consistent mass		
1.00	conv.	conv.	conv.	conv.
		GEMM+ξ lumped mass		
1.00	conv.	conv.	conv.	conv.

Table 4: Maximum level of the dissipation at the end of each analysis.

ρ_∞	C^1	C^2	C^3	C^4
		Gα consistent mass		
0.50	$1 \cdot 10^{-1}\%$	$1 \cdot 10^{-1}\%$	$1 \cdot 10^{-1}\%$	$1 \cdot 10^{-1}\%$
0.95	$2 \cdot 10^{-4}\%$	$2 \cdot 10^{-4}\%$	$2 \cdot 10^{-4}\%$	$1 \cdot 10^{-4}\%$
0.99	$8 \cdot 10^{-4}\%$	$1 \cdot 10^{-4}\%$	$8 \cdot 10^{-4}\%$	$3 \cdot 10^{-3}\%$
1.00	0%	0%	0%	0%
		Gα lumped mass		
1.00	0.44%	0.42%	0.32%	0.39%
		GEMM+ξ consistent mass		
1.00	$4 \cdot 10^{-3}\%$	$3 \cdot 10^{-3}\%$	$\uparrow 1 \cdot 10^{-2}\%$	$\uparrow 8 \cdot 10^{-2}\%$
		GEMM+ξ lumped mass		
1.00	0.45%	0.42%	0.37%	0.17%
		$\uparrow$ implies in the growing of the total energy.		

(a) $\rho_\infty = 0.95$ e C^4 (b) $\rho_\infty = 0.95$ e C^4

Figure 2: Successive configurations: Gα.

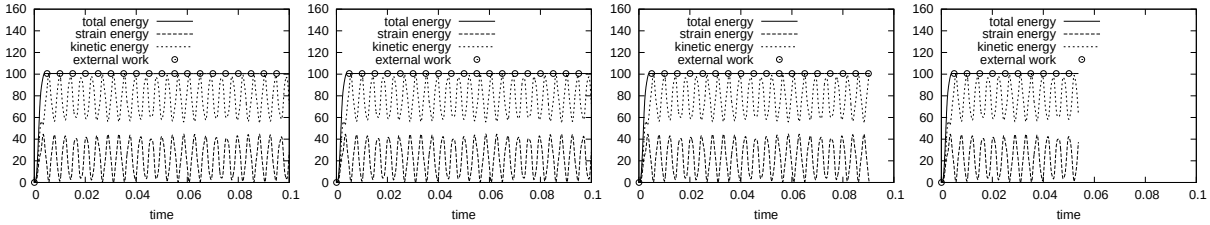

(a) $\rho_\infty = 0.50$, C^4 (b) $\rho_\infty = 0.95$, C^4 (c) $\rho_\infty = 0.99$, C^4 (d) $\rho_\infty = 1.00$, C^4

Figure 3: Energy of toss rule; Gα with consistent mass.

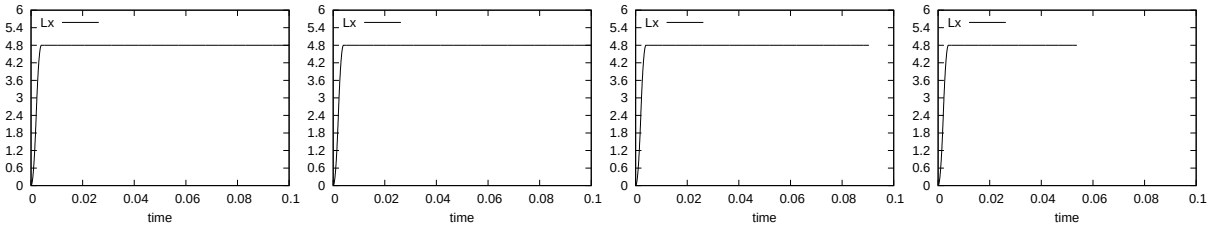

(a) $\rho_\infty = 0.50$, C^4 (b) $\rho_\infty = 0.95$, C^4 (c) $\rho_\infty = 0.99$, C^4 (d) $\rho_\infty = 1.00$, C^4

Figure 4: Linear momentum of toss rule, $\underline{\mathbf{L}}$; Gα with consistent mass.

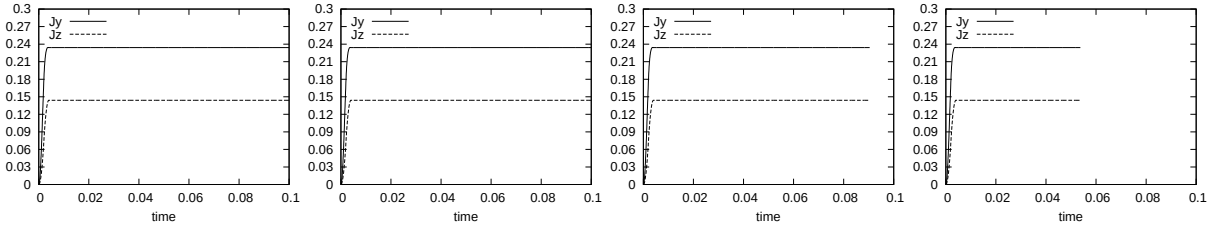

(a) $\rho_\infty = 0.50$, C^4 (b) $\rho_\infty = 0.95$, C^4 (c) $\rho_\infty = 0.99$, C^4 (d) $\rho_\infty = 1.00$, C^4

Figure 5: Angular momentum of toss rule, $\underline{\mathbf{J}}$; Gα with consistent mass.

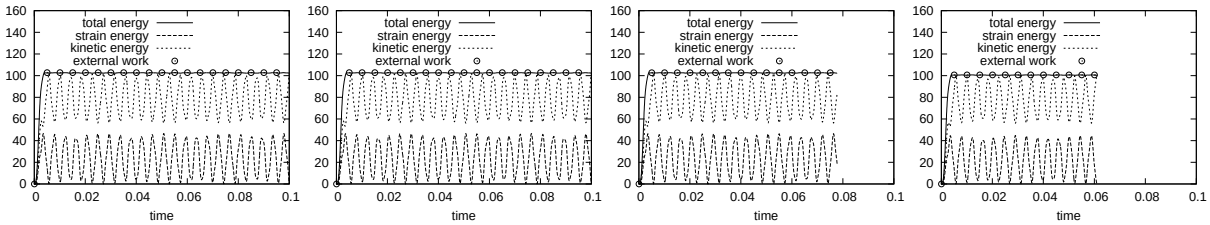

(a) $\rho_\infty = 1.00$, C^1 (b) $\rho_\infty = 1.00$, C^2 (c) $\rho_\infty = 1.00$, C^3 (d) $\rho_\infty = 1.00$, C^4

Figure 6: Energy of toss rule; Gα with lumped mass.

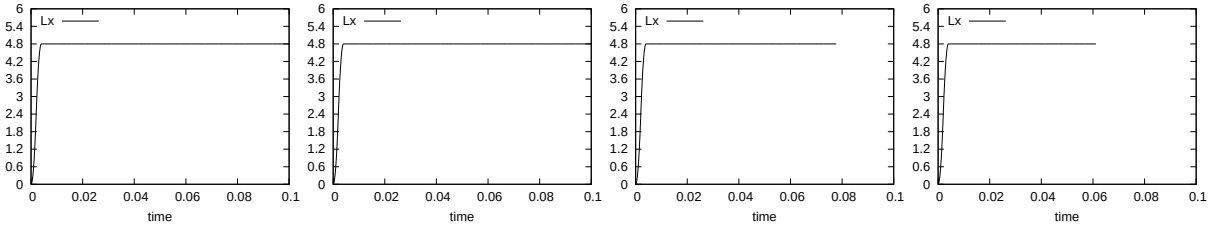

(a) $\rho_\infty = 1.00$, C^1 (b) $\rho_\infty = 1.00$, C^2 (c) $\rho_\infty = 1.00$, C^3 (d) $\rho_\infty = 1.00$, C^4

Figure 7: Linear momentum of toss rule, $\underline{\mathbf{L}}$; Gα with lumped mass.

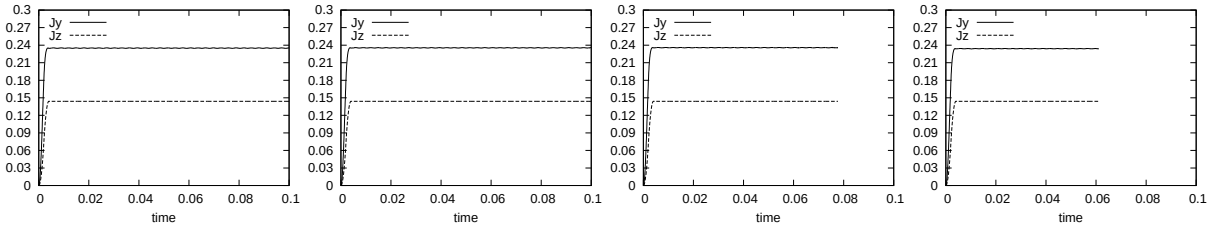

(a) $\rho_\infty = 1.00$, C^1 (b) $\rho_\infty = 1.00$, C^2 (c) $\rho_\infty = 1.00$, C^3 (d) $\rho_\infty = 1.00$, C^4

Figure 8: Angular momentum of toss rule, $\underline{\mathbf{J}}$; Gα with lumped mass.

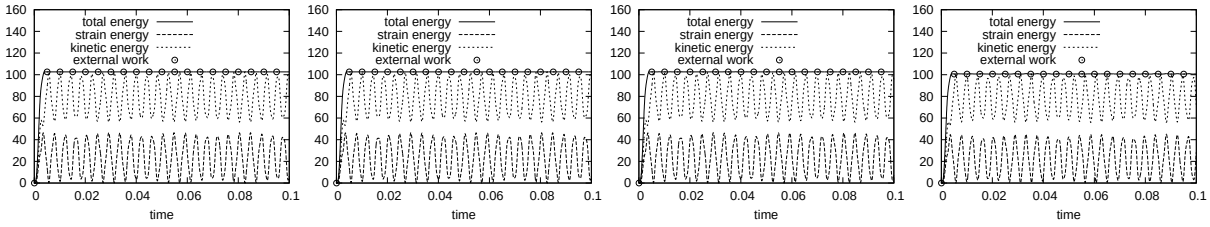

(a) $\rho_\infty = 1.00$, C^1 (b) $\rho_\infty = 1.00$, C^2 (c) $\rho_\infty = 1.00$, C^3 (d) $\rho_\infty = 1.00$, C^4

Figure 9: Energy of toss rule; GEMM+ξ with consistent mass.

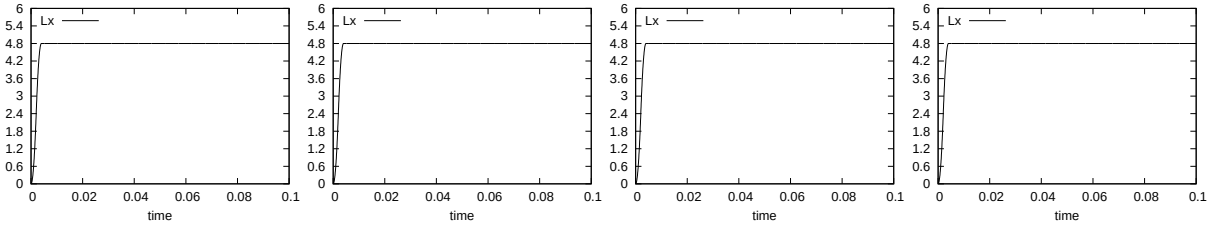

(a) $\rho_\infty = 1.00$, C^1 (b) $\rho_\infty = 1.00$, C^2 (c) $\rho_\infty = 1.00$, C^3 (d) $\rho_\infty = 1.00$, C^4

Figure 10: Linear momentum of toss rule, $\underline{\mathbf{L}}$; GEMM+ξ with consistent mass.

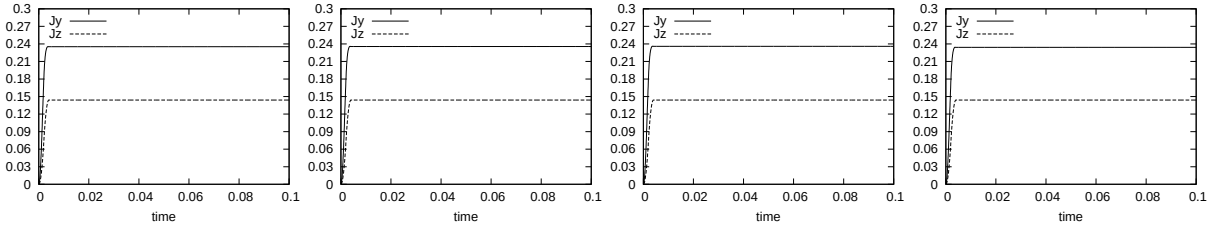

(a) $\rho_\infty = 1.00$, C^1 (b) $\rho_\infty = 1.00$, C^2 (c) $\rho_\infty = 1.00$, C^3 (d) $\rho_\infty = 1.00$, C^4

Figure 11: Angular momentum of toss rule, $\underline{\mathbf{J}}$; GEMM+ξ with consistent mass.

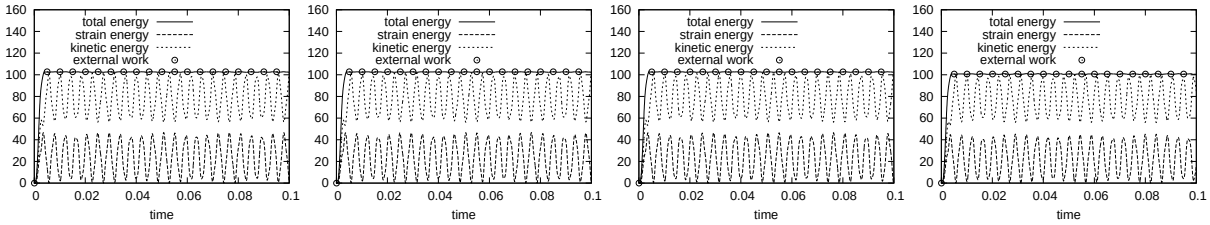

(a) $\rho_\infty = 1.00$, C^1 (b) $\rho_\infty = 1.00$, C^2 (c) $\rho_\infty = 1.00$, C^3 (d) $\rho_\infty = 1.00$, C^4

Figure 12: Energy of toss rule; GEMM+ξ with lumped mass.

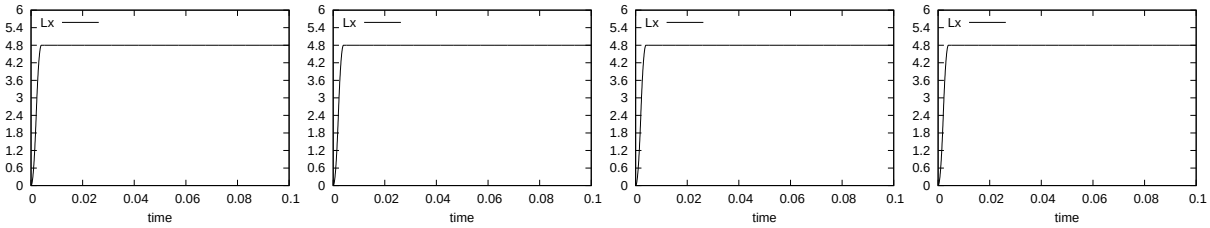

(a) $\rho_\infty = 1.00$, C^1 (b) $\rho_\infty = 1.00$, C^2 (c) $\rho_\infty = 1.00$, C^3 (d) $\rho_\infty = 1.00$, C^4

Figure 13: Linear momentum of toss rule, $\underline{\mathbf{L}}$; GEMM+ξ with lumped mass.

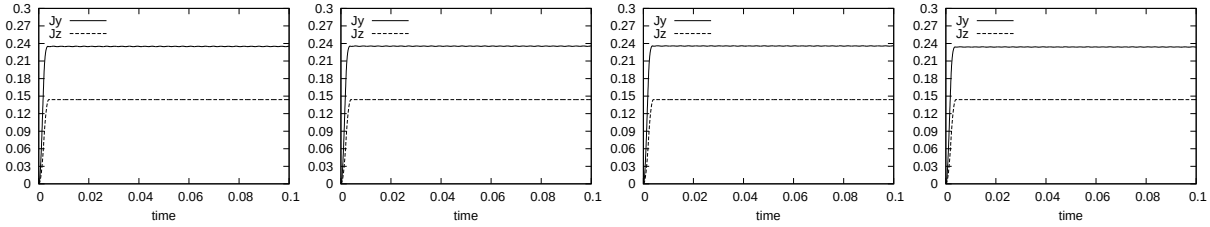

(a) $\rho_\infty = 1.00$, C^1 (b) $\rho_\infty = 1.00$, C^2 (c) $\rho_\infty = 1.00$, C^3 (d) $\rho_\infty = 1.00$, C^4

Figure 14: Angular momentum of toss rule, $\underline{\mathbf{J}}$; GEMM+ξ with lumped mass.

3.2 "Snap-Through" of cylindrical shell

The snap-through phenomenon occurring in a hinge-supported cylindrical shell subject to a concentrated load is investigated here. Geometry and boundary conditions are shown in Figure 15a, load description for the present simulation are shown in Figure 15b and material properties of the structure as well as the time step adopted in the time integration procedure are found in Table 5. Information on computational parameters utilized in the parametric studies carried out here are summarized in Table 6. Number and distribution (L, w, h) of elements over the physical space referring to the cylindrical shell are given as follows: the continuity class C^1 corresponds to the continuity class employed over the shell surface, where the element configuration (8×8) is adopted. The computational mesh related to the continuity class C^4 presents (4×4) elements over the shell surface. Along the shell thickness, two elements of C^0 continuity are used in both meshes, such that the control points associated with the middle surface of the cylindrical shell become interpolatory and the boundary conditions corresponding to hinge supports can be appropriately imposed.

Figures 17, 19 present results in term of energies for Gα method and GEMM+ξ method with consistent mass, respectively. Figures 18, 20 present the dynamic responses which are given in terms of vertical displacements measured at the position where the load is applied. In addition, the displacement response is also evaluated at the middle point on the free edge of the cylindrical shell.

One can observe that the continuity class has a minor influence on the dynamic responses obtained here. On the other hand, the effects induced by the spectral radius are clearly noted, since the displacements are continuously increasing for $\rho_\infty = 0.90$ and $\rho_\infty = 0.95$. A stable solution is obtained for $\rho_\infty = 0.50$ for Gα method, although numerical damping can be also observed. For GEMM+ξ a stable solution is obtained for $\rho_\infty = 0.95$, however an excessive amount of numerical dissipation is observed. Nevertheless, the amount of numerical damping must be carefully controlled in order to obtain accurate results.

In Figure 21a, results obtained in this work are compared with numerical predictions obtained by Kuhl and Ramm (1999) and the commercial package ABAQUS (explicit solver), while in Figure 21b it is compared with Balah and Al-Ghamedy (2005); Kuhl and Ramm (1996). In Figure 21c is compared Gα and GEMM+ξ methods. The present results correspond to the numerical analysis performed considering a spectral radius and and continuity class of $\rho_\infty = 0.50$, C^4 and $\rho_\infty = 0.95$, C^4 for Gα and GEMM+ξ methods. A good agreement can be observed, except for the solution presented by Kuhl and Ramm (1999), where the higher modes are not present and the energy is concentrated on the lower modes.

It was observed that the convergence rate of this analysis is about 1.5 and 2.0 for force and displacement convergence, respectively, in Gα method, while in GEMM+ξ method is observed a convergence rate about 1.7 and 2.0 for force and displacement convergence, respectively.

In Figure 22 is shown the dissipation evolution along the time. It is important to note that there is an increase in the numerical dissipation (i.e. the external work is greater than total energy), when the analysis is dominated by lower frequencies, in the simulations carried out with GEMM+ξ method. Nevertheless, it is stable, while for Gα the instability is notorious.

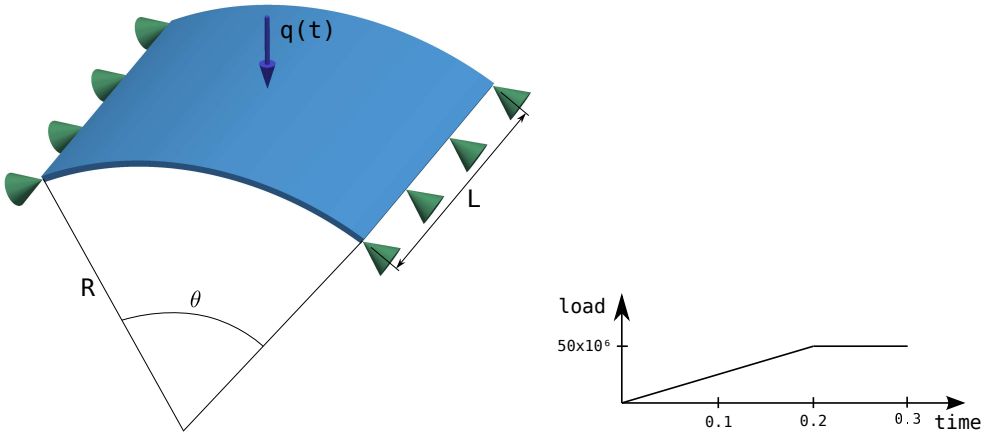

(a) Geometry and boundary conditions (b) Load

Figure 15: Geometry and boundary conditions of cylindrical shell.

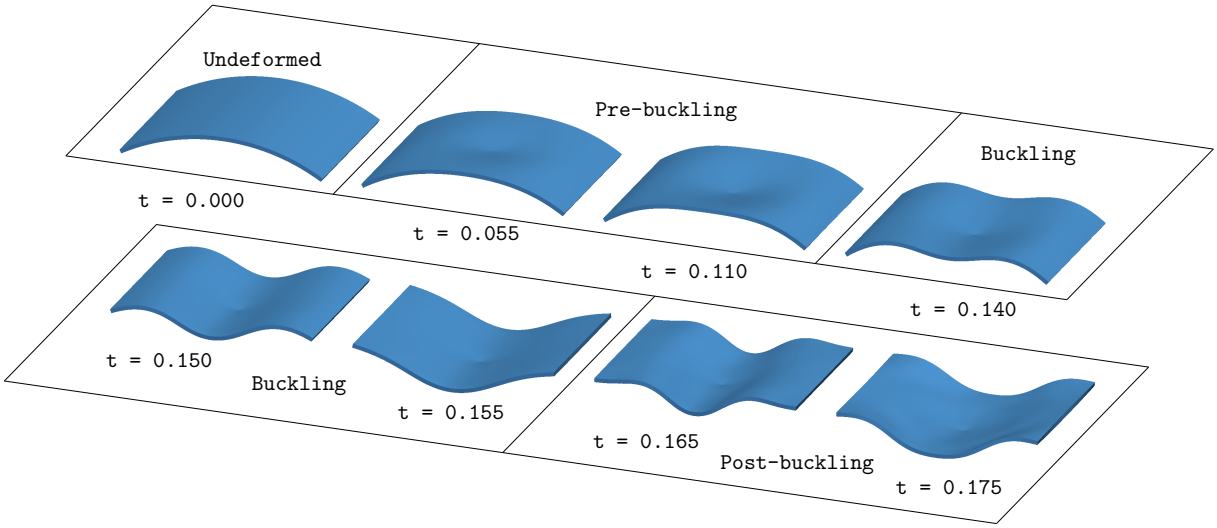

Figure 16: Successive configurations: Gα.

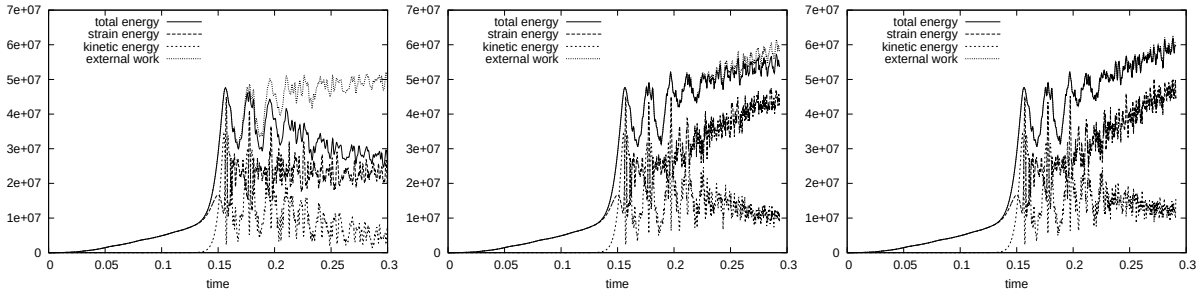

(a) $\rho_\infty = 0.50$, C^1 (b) $\rho_\infty = 0.90$, C^1 (c) $\rho_\infty = 0.95$, C^1

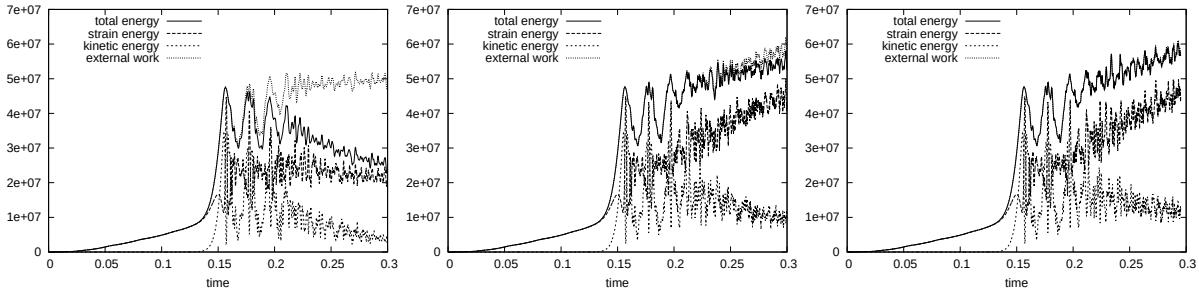

(d) $\rho_\infty = 0.50$, C^4 (e) $\rho_\infty = 0.90$, C^4 (f) $\rho_\infty = 0.95$, C^4

Figure 17: Energy of cylindrical shell; Gα consistent mass.

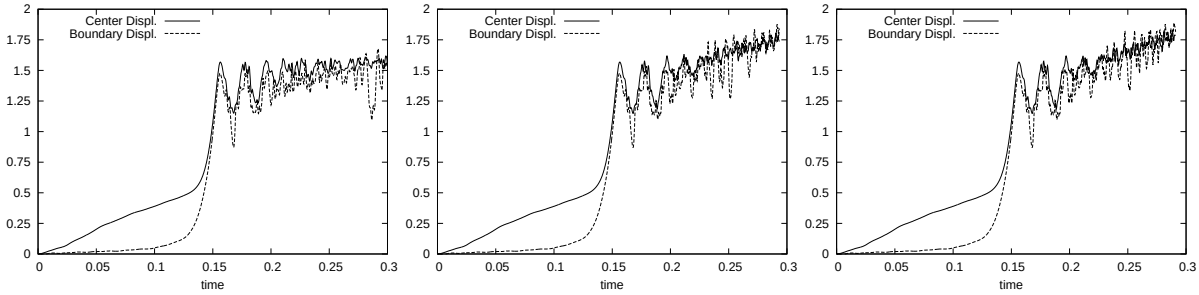

(a) $\rho_\infty = 0.50$, C^1 (b) $\rho_\infty = 0.90$, C^1 (c) $\rho_\infty = 0.95$, C^1

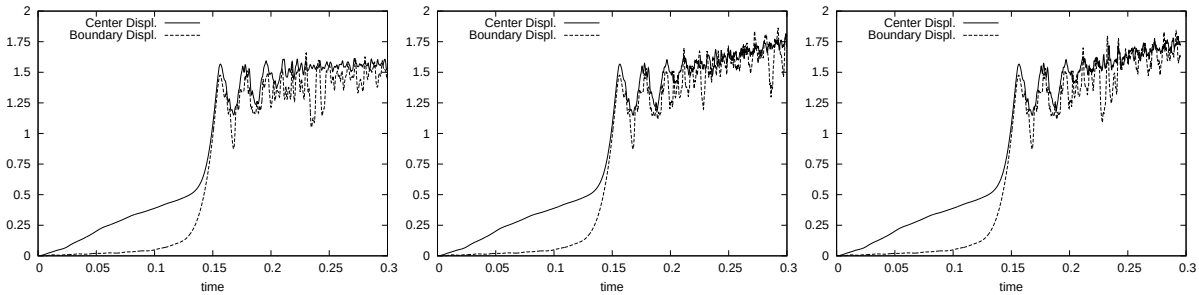

(d) $\rho_\infty = 0.50$, C^4 (e) $\rho_\infty = 0.90$, C^4 (f) $\rho_\infty = 0.95$, C^4

Figure 18: Displacement at point load location of cylindrical shell; Gα consistent mass.

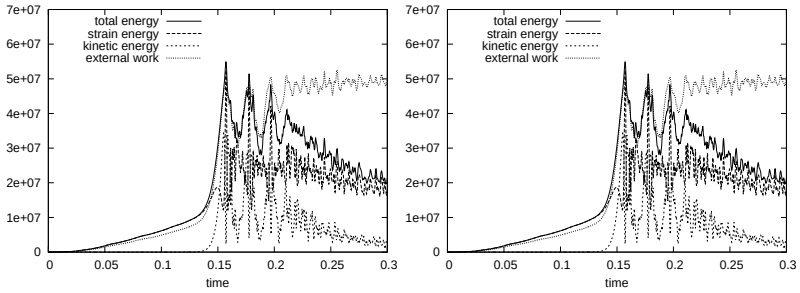

(a) $\rho_\infty = 0.90$, C^1 (b) $\rho_\infty = 0.90$, C^4

(c) $\rho_\infty = 0.95$, C^1 (d) $\rho_\infty = 0.95$, C^4

Figure 19: Energy of cylindrical shell; GEMM+ξ consistent mass.

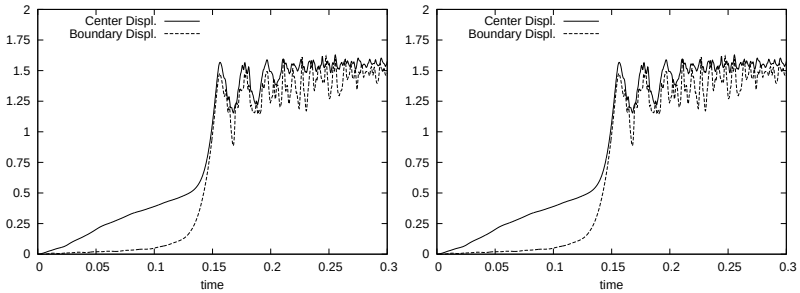

(a) $\rho_\infty = 0.90$, C^1 (b) $\rho_\infty = 0.90$, C^4

(c) $\rho_\infty = 0.95$, C^1 (d) $\rho_\infty = 0.95$, C^4

Figure 20: Displacement at point load location of cylindrical shell; GEMM+ξ consistent mass.

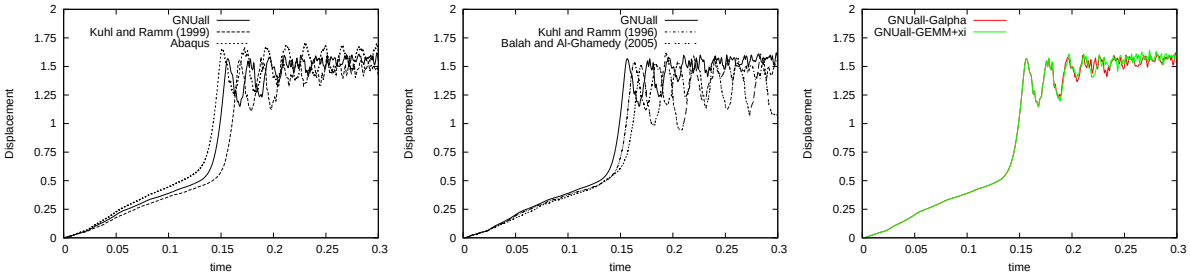

(a) comparison 1 (b) comparison 2 (c) comparison 3

Figure 21: Comparisons of vertical displacement of the middle point.

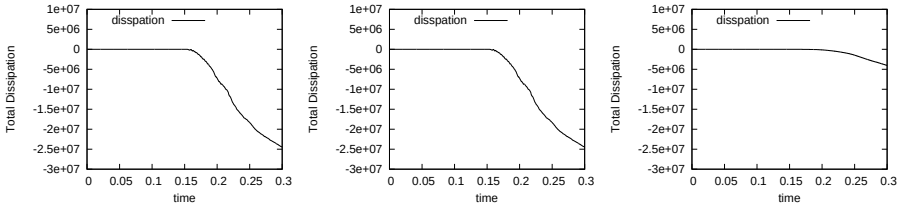

(a) Gα, C^1, $\rho_\infty = 0.50$(b) Gα, C^4, $\rho_\infty = 0.50$(c) Gα, C^1, $\rho_\infty = 0.90$

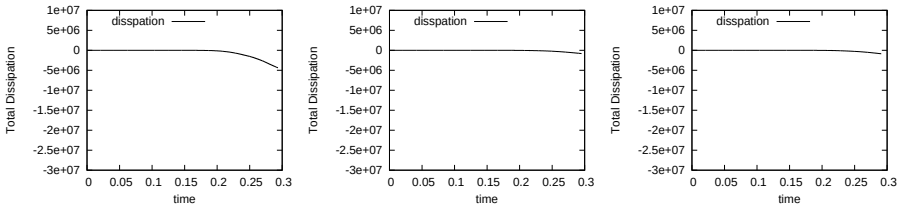

(d) Gα, C^4, $\rho_\infty = 0.90$(e) Gα, C^1, $\rho_\infty = 0.95$(f) Gα, C^4, $\rho_\infty = 0.95$

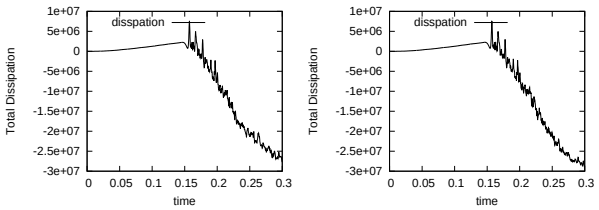

(g) GEMM+ξ, C^1,(h) GEMM+ξ, C^4,
$\rho_\infty = 0.90$ $\rho_\infty = 0.90$

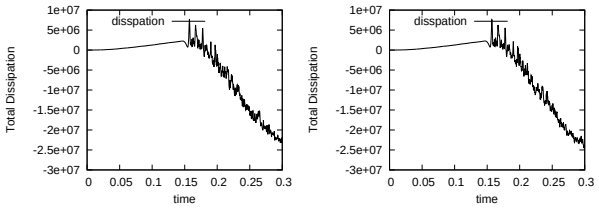

(i) GEMM+ξ, C^1,(j) GEMM+ξ, C^4,
$\rho_\infty = 0.95$ $\rho_\infty = 0.95$

Figure 22: Dissipation in Gα vs dissipation in GEMM+ξ.

Table 5: Geometrical and load characteristics for the cylindrical shell analysis

Young modulus - $E\left[N/m^2\right]$	$2.0 \cdot 10^{11}$
Poisson coefficient - ν	0.25
Specific mass - $\rho\left[kg/m^3\right]$	$1.0 \cdot 10^4$
Damping coefficient - ϕ	0.0
Time step - $\Delta t\,[s]$	$5.0 \cdot 10^{-4}$

Table 6: Computational parameters employed in the cylindrical shell analysis

Control mesh (L, h, z)	Continuity class	Spectral radius - ρ_∞	Degrees (p, q, r)
	Gα consistent mass		
$18 \times 18 \times 5$	C^1	$0.50; 0.90; 0.95$	$5, 5, 2$
$13 \times 13 \times 5$	C^4	$0.50; 0.90; 0.95$	$5, 5, 2$
	GEMM+ξ consistent mass		
$18 \times 18 \times 5$	C^1	$0.90; 0.95$	$5, 5, 2$
$13 \times 13 \times 5$	C^4	$0.90; 0.95$	$5, 5, 2$

Table 7: Convergence and failure time.

ρ_∞	C^1	C^4
	Gα consistent mass	
0.50	conv.	conv.
0.90	conv.	fail at $t_f = 0.2934s$
0.95	fail at $t_f = 0.2952s$	fail at $t_f = 0.2910s$
	GEMM+ξ consistent mass	
1.00	conv.	conv.

Table 8: Maximum level of the dissipation at the end of each analysis.

ρ_∞	C^1	C^4
	Gα consistent mass	
0.50	51%	47%
0.90	7%	8%
0.95	1%	1%
	GEMM+ξ consistent mass	
0.90	64%	57%
0.95	46%	46%
$\uparrow$ implies in the growing of the total energy.		

4 CONCLUSIONS

The improvement provided by the NURBS basis functions has a great impact over the conserving energy-momentum budget and numerical stability. Also, the deterioration of solution implied by the lumped mass is indistinguishable from the consistent mass.

Although the GEMM+ξ method present a better stability with respect to Gα method, the energy budget obtained with the GEMM+ξ method shows a very slight oscillation, even for the consistent mass.

In Kuhl and Ramm (1996); Kuhl and Crisfield (1999); Kuhl and Ramm (1999) the Gα method is presented as a dissipative and unstable time integrator, and the numerical stability and the energy-momentum conserving are related only to the time integrator. In the analyses carried out here is evident that the basis of the spatial discretization is so important as the integrator. Actually, the continuity class has a major role in the stability and energy-momentum conserving.

5 ACKNOWLEDGMENTS

The authors wish to thank to CAPES and CNPq (Brazilian Research Committees) for their financial support and they thank also to CESUP (UFRGS Supercomputing Center) for its important contributions.

REFERENCES

Armero F. and Petocz E. Formulation and analysis of conserving algorithms for frictionless dynamic contact-impact problems. *Computer Methods in Applied Mechanics and Engineering*, Vol. 158:269–300, 1998.

Armero F. and Romero I. On the formulation of high-frequency dissipative time-stepping algorithms for nonlinear dynamics. part i: low order methods for two model problems and nonlinear elastodynamics. *Computer Methods in Applied Mechanics and Engineering*, Vol. 190:2603–2649, 2001a.

Armero F. and Romero I. On the formulation of high-frequency dissipative time-stepping algorithms for nonlinear dynamics. part ii: high order methods. *Computer Methods in Applied Mechanics and Engineering*, Vol. 190:6783–6824, 2001b.

Balah M. and Al-Ghamedy H.N. Energy–momentum conserving algorithm for nonlinear dynamics of laminated shells based on a third-order shear deformation theory. *Journal Of Engineering Mechanics ASCE*, Vol. 131:12–22, 2005.

Bathe K.J. *Finite Element Procedures*. Prentice Hall, 2th edition, 1996.

Bazilevs Y., Calo V., Cottrell J., Hughes T., Reali A., and Scovazzi G. Variational multiscale residual-based turbulenve modeling for large eddy simulation of incompressible flows. *Computer Methods in Applied Mechanics and Engineering*, Vol. 197:173–201, 2007.

Belytschko T. and Schoeberle D. On the unconditional stability of an implicit algorithm for nonlinear structural dynamics. *ASME Journal of Applied Mechanics*, Vol. 17:865–869, 1975.

Benson D., Bazilevs Y., Hsu M., and Hughes T. Isogeometric shell analysis: The reissner-mindlin shell. *Computer Methods in Applied Mechanics and Engineering*, Vol. 199:276–289, 2010.

Braun A. and Awruch A. Geometrically non-linear analysis in elastodynamics using the

eight-node finite element with one-point quadrature and the generalized-α method. *Latin American Journal of Solids and Structures*, Vol. 5:17–45, 2008.

Chung J. and Hulbert G. A time integration algorithm for structural dynamics with improved numerical dissipation: the generalized-α method. *Journal of Applied Mechanics, Transactions of the ASME*, Vol. 60:371–375, 1993.

Cottrell J., Hughes T., and Bazilevs Y. *Isogeometric Analysis: Towards Integration of CAD and FEA*. Wiley, 2009.

Cox M. The numerical evaluation of B-spline. *Inst. Math. Applic.*, Vol. 10(1):134–149, 1972.

Crisfield M., Galvanetto U., and Jelenic G. Dynamics of 3-d co-rotational beams. *Computational Mechanics*, Vol. 20:507–519, 1997.

deBoor C. On calculating with B-spline. *Approx. theory*, Vol. 6(1):50–72, 1972.

Erlicher S., Bonaventura L., and Bursi O. The analysis of the generalized-α method for non-linear dynamic problems. *Computational Mechanics*, Vol. 28:83–104, 2002.

Gonzalez G. Exact energy and momentum conserving algorithms for general models in nonlinear elasticity. *Computer Methods in Applied Mechanics and Engineering*, Vol. 190:1763–1783, 2000.

Goudreau G. and Taylor R. Evaluation of numerical methods in elastodynamics. *Computer Methods in Applied Mechanics and Engineering*, Vol. 2:69–97, 1973.

Hilber H., Hughes T., and Taylor R. Improved numerical dissipation for the time integration algorithms in structural dynamics. *Earthquake Engineering and Structural Dynamics*, Vol. 5:283–292, 1977.

Hughes T., Caughey T., and Liu W. Finite element methods for nonlinear elastodynamics which conserve energy. *Journal of Applied Mechanics*, Vol. 45:366–370, 1978.

Hughes T. and Winget J. Finite rotations effects in numerical integration of rate construtive equations arising in large deformation analysis. *International Journal for Numerical Methods in Engineering*, Vol. 15:1862–1867, 1980.

Kiendl D., Bazilevs Y., Hsu M., Wüchner R., and Bletzinger K. The bending strip method for isogeometric analysis of kirchhoff-love shell structures comprised of multiple patches. *Computer Methods in Applied Mechanics and Engineering*, Vol. 199:2403–2416, 2010.

Kuhl D. and Crisfield M. Energy-conserving and decaying algorithms in non-linear structural dynamics. *International Journal for Numerical Methods in Engineering*, Vol. 45:569–599, 1999.

Kuhl D. and Ramm E. Constraint energy momentum algorithm and its application to nonlinear dynamics of shells. *Computer Methods in Applied Mechanics and Engineering*, Vol. 136:293–315, 1996.

Kuhl D. and Ramm E. Generalized energy-momentum method for non-linear adaptive shell dynamics. *Computer Methods in Applied Mechanics and Engineering*, Vol. 178:343–366, 1999.

Laursen T. and Meng X. A new solution procedure for application of energy-conserving algorithms to general constitutive models in nonlinear elastodynamics. *Computer Methods in Applied Mechanics and Engineering*, Vol. 190:6309–6322, 2001.

Malvern L. *Introduction to the Mechanics of a Continuous Medium*. Prentice Hall, 1969.

Newmark N. A method of computation for structural dynamics. *Journal of Engineering Mechanics ASCE*, Vol. 85-EM3:67–94, 1959.

Noels L., Stainier L., and Ponthot J. An energy-momentum conserving algorithm for nonlinear hypoelatic constitutive models. *International Journal for Numerical Methods in*

Engineering, Vol. 59:83–114, 2004.

Ortiz M. A note on energy conservation and stability of nonlinear time-stepping algorithms. *Computer and Structures*, Vol. 24:167–168, 1986.

Piegl L.A. and Tiller W. *The Nurbs Book*. Springer, 2^{nd} edition, 1997.

Romero I. An analysis of the stress formula for energy-momentum methods in nonlinear elastodynamics. *Computational Mechanics*, Vol. 50:603–610, 2012.

Simo J. and Tarnow N. The discrete energy-momentum method, conserving algorithms for nonlinear elastodynamics. *Journal of Applied Mathematics and Physics*, Vol. 43:757–792, 1992.

Wood W., Bossak M., and Zienkiewicz O. An alpha modification of newmark's method. *International Journal for Numerical Methods in Engineering*, Vol. 15:1562–1566, 1980.